Norwegian University of Life Sciences

Master's thesis 2025 45 ECTS
MINA

An evaluation of the quantification of mineral content using SlateNorm software

Stian Hassum
Environmental Science

Abstract

This study explores applying mineral norm calculations to evaluate the reliability of determining shale mineral composition from whole-rock geochemical analysis. Understanding the mineralogical composition of shales like alum shale, known for high heavy metal/organic content and acid-producing capabilities (acid rock drainage), is critical for assessing shale related environmental risks and geotechnical challenges. While traditional methods like X-ray diffraction (XRD) can be both time-consuming and expensive, mineral norm calculations offer a potentially cheaper alternative. In this study, the practicality and accuracy of an existing norm calculation method originally developed for roofing-slate assessments, SlateNorm (Wagner et al., 2020), which estimates mineralogy from whole-rock geochemical composition was tested and compared with associated quantitative XRD mineral compositions. Data were compiled from four published shale datasets, consisting of 150 samples in total. The geochemical data required modifications (documented in this study) to meet SlateNorm input requirements. SlateNorm outputs were compared against XRD results using absolute relative difference, Lin's Concordance Correlation Coefficient (r_c), and a whole-dataset scatterplot showing absolute relative difference between SlateNorm and XRD plotted against XRD wt.% for each mineral within each sample (mineral-sample pair), including a modified accuracy threshold. Results indicated SlateNorm calculations deviated significantly from XRD, with a total of nearly one third (31%) of mineral-sample pairs exceeding the established accuracy threshold. Systematic over- and under-estimations (chlorite, clays) and large, erratic errors for quartz, feldspar, and pyrite were common. Lin's r_c values were generally poor (mostly <0.70), indicating weak concordance with XRD. SlateNorm's relatively poor performance is likely due to algorithm limitations (e.g., ignoring structural water (H_2O^+), applying assumptions more suited for roofing slates) and potentially also due to the necessary input data modifications. As a result, SlateNorm, in its current form is not considered a practical tool for reliable shale mineral identification, quantification, or assessing ARD potential based on its mineralogical output. Future work should address algorithm limitations (e.g., incorporating H_2O^+ for input, and pyrrhotite output) and validate against high-resolution methods. The overall most reliable method probably still involves Automated Mineralogy Systems described in Chapter 4.2, and despite time and cost requirements it might be useful to apply these systems, even at a smaller scale, to evaluate their usefulness for shale (e.g., alum shale) mineral quantification.

Acknowledgement

I would like to give a huge thanks to my thesis supervisor, Jan Marten Huizenga, for providing great input and guidance throughout this last year. His consistent support and quick replies whenever I had questions were much appreciated and made working on this project a much better experience.

I am also really thankful for having friends and family who have encouraged and supported me during tougher times.

Table of contents

List of figures

List of tables

List of appendices

Appendix A: Overview of compiled geochemical and XRD data, SlateNorm inputs and outputs, and numerical values of comparison results

Appendix B: Overview of generated charts and comparison figures

Appendix C: Overview of calculation steps in SlateNorm algorithm

Appendix D: Compilation of SlateNorm input and output files generated in this study

All appendices are available for download at: Appendix A-D.zip

1. Introduction

This study explores the application of mineral norm calculations to evaluate the reliability of determining shale mineral composition from whole-rock geochemical analysis. This is in particular relevant for the alum shale in Norway, which could potentially impact negatively on the environment and pose engineering challenges (e.g., Pabst et al., 2016).

Alum shale, a geological formation prevalent in Scandinavia, is known for its high metal and organic matter content, and its acid producing capabilities. This process is commonly known as acid rock drainage (ARD), and it occurs in certain black shales due to the presence of sulphide minerals, such as pyrite and pyrrhotite (Bjørlykke, 1974). Sulphide minerals exposed to oxygen and water, e.g., in regions where alum shales are disturbed by mining, construction, or natural weathering, undergo oxidation to produce sulphuric acid. This process can lead to the acidification of soil and water, posing threats to ecosystems and human health (Dold, 2017).

The mineralogical composition of these rocks also affects their mechanical properties, particularly their brittleness and susceptibility to weathering. Brittleness influences fracture patterns and hydraulic conductivity, which can facilitate water infiltration and accelerate the oxidation of sulphide minerals (Bailey et al., 2022). As a result, construction activities in areas underlain by black shales may encounter issues such as ground instability, and structural damage (Pabst et al., 2016).

Understanding the mineralogical composition of black shales is therefore critical to assessing their environmental risks and potential geotechnical challenges. By quantifying key acid producing minerals, such as sulphides, and acid-neutralizing carbonates, and the strength-controlling minerals that dictate brittleness or ductility (e.g., quartz, feldspars, clays), it is possible to better predict their behaviour under varying conditions and develop strategies to mitigate potential impacts.

Shale mineralogical characterization and quantification has historically posed significant challenges due to its fine-grained texture complicating the identification of minerals using conventional petrographic methods (Lou et al., 2020). Alternative methods such as X-ray diffraction (XRD) are not straightforward, time consuming, and expensive. By utilizing mineral norm calculations there is potential for accurate and detailed analysis, predicting mineral composition from the chemical composition of rock samples, which is comparatively cheaper than most established whole-rock mineral analysis methods.

This research will focus on testing the practicality and accuracy of an existing norm calculation method called *SlateNorm* (Wagner et al., 2020), which calculates sample mineralogical composition directly from its whole-rock geochemical composition.

Major element whole-rock geochemical data and mineral compositions of shales have been published in the literature and are readily available. This research will include the following: (1) Geological background of alum shale in Norway and its associated environmental issues; (2) Description of the importance of mineralogical characterization of alum shale; (3) Literature review of established mineralogical characterization methods and their limitations; (4) Overview of SlateNorm calculation method and its related software; (5) Identification and quantification of the mineralogical content of available shale datasets using SlateNorm; (6) Compilation of data and comparison results used in this study in external appendices, available for download at the following pCloud link: Appendix A-D.zip; (7) Discussion of results.

2. Geological setting

The black shale units found in the Oslo Region of southeastern Norway (Fig. 1) were deposited during the Paleozoic era, during which this area was part of the Baltica continental plate. The following section describes key geological events that contributed to the formation and preservation of these shale units. A brief overview of the associated stratigraphy is also included (Fig 2). The geological context outlined in this chapter mainly follows Nakrem and Worsley (2013) and references within their work, with additional citations specified where relevant.

2.1. Regional geology of the Oslo Region

The Oslo Region ("Oslofeltet") is a roughly 220 km long and 60 km wide triangular, mostly subsided area that extends north-northeast from Langesund to Mjøsa (Fig. 1). Due to its tectonic and magmatic evolution, the Lower Paleozoic stratigraphy (i.e., black shale, lime-stone and sandstone units) in this region has been well preserved, unlike the remainder of Norway, where these sedimentary units experienced extensive erosion or metamorphic alteration during the Caledonian Orogeny from approximately 455 to 405 million years ago (Ma).

The preservation of these units is largely attributed to the Oslo Rift, a large-scale rift basin (graben) formed by extensional tectonics in the region (e.g., Nakrem and Worsley, 2013; Ro et al., 1990). The Oslo rift began forming in the upper Carboniferous period and continued developing into the Permian period (310–250 Ma). The rifting was primarily driven by (1) a period of volcanic eruptions and earthquakes alongside heating of the crust and (2) extensional tectonic forces following the Hercynian (Variscan) orogeny (380-280 Ma; Hurum and Frøyland, 2004), which occurred as the northern continents, including Baltica, collided with Gondwana during the assembly of the Pangea continent. This resulted in western and southern Norway being pulled westward, while eastern Norway and Sweden were pulled eastward. The extensional movement led to the development of north-south trending normal faults that shaped the rift valley in the Oslo Region. Within the rift, blocks of Paleozoic sedimentary rocks subsided along faults, preserving the stratigraphic record (Hurum and Frøyland, 2004). Volcanic activity further contributed to preservation and the geological complexity of the region, with magma flows filling fractures and solidifying into various igneous rocks in the region (Hurum and Frøyland, 2004; Fig.1).
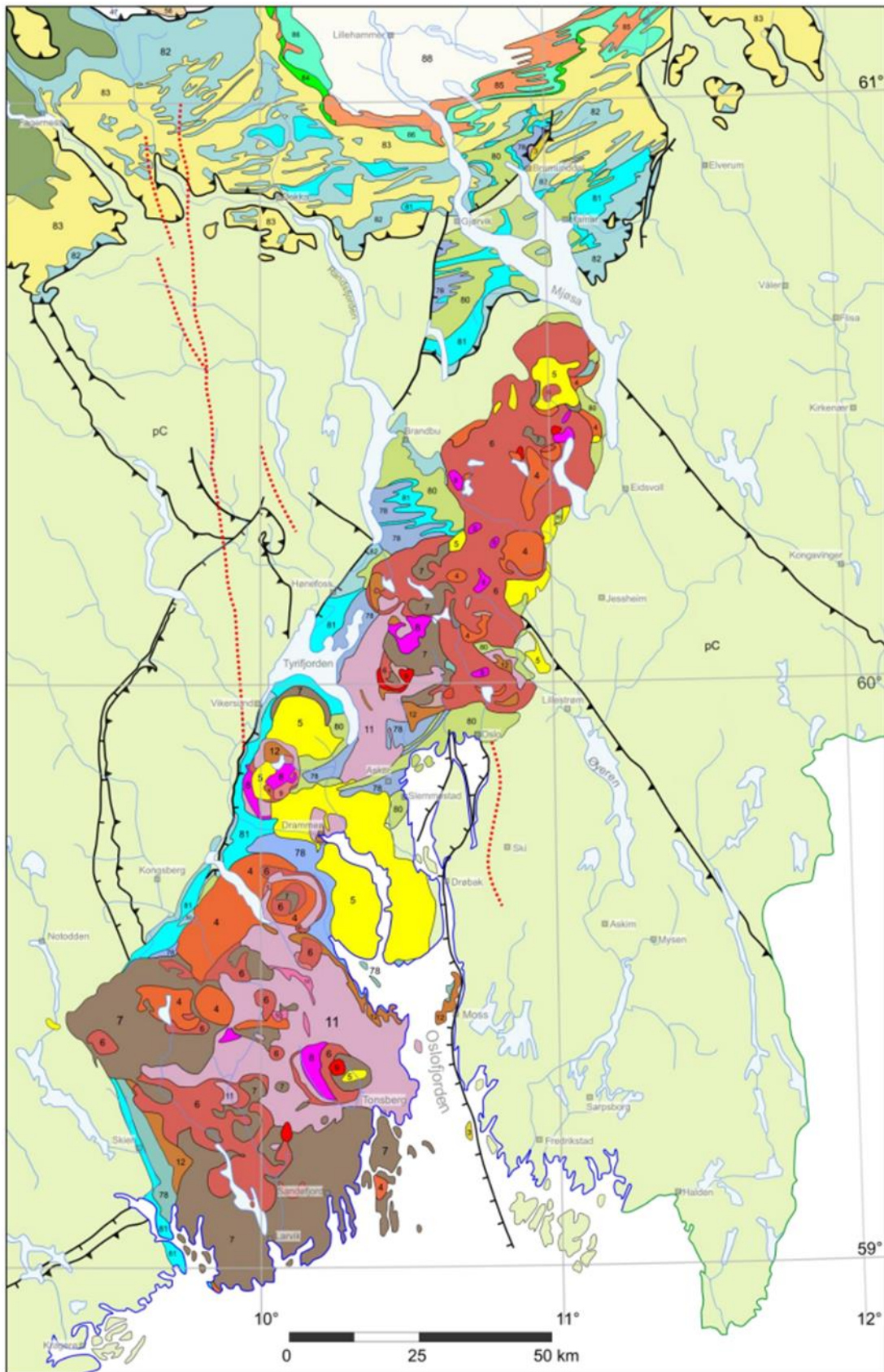
Figure 1: *Geological map and legend (on the following page) for the Oslo Region. Map modified by Jan Marten Huizenga (unpublished) from the Geological Survey of Norway (2021).*

Igneous and sedimentary rocks associated with the Oslo rift [320-250 Ma]

- 3   Conglomerate, sandstone, claystone [280-250 Ma]
- 4   K-feldspar granite [280-255 Ma]
- 5   Granite, granodiorite [290-255 Ma]
- 6   Quartz-K-feldspar syenite to nepheline syenite [295-255 Ma]
- 7   Monzonite (larvikite), monzodiorite, syenite [300-265 Ma]
- 8   Rhyolite to trachyte, latite, basalt [280-270 Ma]
- 9   Volcanic breccia, tuff, agglomerate, ignimbrite [300-250 Ma]
- 10   Trachite [300-250 Ma]
- 11   Latite (rhomb porphyry), sedimentary rocks [300-280 Ma]
- 12   Basalt, sedimentary rocks [320-295 Ma]
- ·····   Rhomb porphyry, mafic dyke [320-250 Ma]

Reverese fault / shear zone

Normal fault / shear zone

Sedimentary rocks [540-450 Ma]

- 78   Limestone, slate, sandstone, conglomerate [440-420 Ma]
- 80   Slate, sandstone, limestone [470-450 Ma]
- 81   Limestone, slate, sandstone [485-470 Ma]
- 82   Limestone, slate, alum shale, sandstone, conglomerate [540-470 Ma]

Sedimentary rocks [750-520 Ma]

- 83   Sandstone, quartzite, .slate, conglomerate [600-520 Ma]

Igneous and metamorphic rocks [1740-910 Ma]

- pC   Precambrian basement rocks

Figure 1: *(Continued)*

2.2. Lower Paleozoic stratigraphy of the Oslo Region

2.2.1. Cambrian

During the early Cambrian period (541–509 Ma) the global sea level started rising. This event was the beginning of the sedimentary record in the Oslo region. By the Middle of the Cambrian period (509–497 Ma) and into the Late Cambrian (497–485 Ma), nearly all of Baltica, including what is now the Oslo region lay beneath a deep ocean. With increasing water depth, the seafloor became stagnant and anaerobic, causing the rate of organic material decomposition to decrease. This led to mud with a high organic content to accumulate and deposit at a seafloor with little to no circulation. These dark deposits are what makes up the bottom part of the Lower Paleozoic stratigraphy. Historically, these rock units were subdivided into "stages" by early geologists (e.g., Theodor Kjerulf in 1857). The previously mentioned unit is the "Alum Shale Formation" and consist of stages 2e and 3a (Fig. 2). In central Oslo, it can measure around 50 meters thick. During the later Caledonian orogeny (455–405 Ma), this relatively "soft" shale acted as a glide plane, deforming it, which has made estimating its original exact thickness complicated (Nakrem and Worsley, 2013).

This black shale unit is named "alum shale" because it historically served as a source for manufacturing potassium-aluminium sulphate ($KAl(SO_4)_2 \cdot 12H_2O$; alum). The shale itself lacks naturally occurring alum, but a long burning process followed by dissolution and crystallization was used to obtain the final product, which was then used for dyeing textiles and leather tanning among other things (Nakrem and Worsley, 2013).

2.2.2. Ordovician

Transitioning into the Ordovician period (ca. 485 Ma) deposition of black mud persisted, but over time the circulation at the seafloor increased slightly, with higher deposition rates leading to the formation of grey to greyish-black shales interspersed with limestone nodules and layers. Further into the Early and Middle Ordovician period, repeated cycles of shale- and limestone-dominated sedimentation indicate fluctuating sea levels. Dark shale intervals point to relatively deep, anaerobic conditions with limited circulation, and the limestone beds correlate with shallower waters. These units have a total thickness of roughly 450m (Fig 2).

Era	Period		Formation	Stage	Thickness	Rock type
Lower Paleozoic	Silurian	Pridoli — 419 Ma	Stubdal	10	750	
		Ludlow	Sundvollen	10	500	
			Steinsfjord	9	260	
		Wenlock	Malmøy	8c-d	35	
			Skinnerbukt	8a-b	90	
			Vik	7c	80	
		Llandovery	Rytteråker	7a-b	50	
			Solvik	6a-c	190	
	Ordovican	Upper — 444 Ma	Langøyene-Langår	5b	50-60,13-35	
			Husbergøy	5a	10-35	
			Skogerholm	4d	33-43	
			Skjerholm	4cγ	35-40	
			Grimsøy	4cβ	10-40	
			Venstøp	4cα	7-10	
			Solvang	4bδ	12-20	
			Nakkholm	4bγ	13-20	
			Frognerkil	4bβ	10-20	
			Arnestad	4bα	22-40	
			Voll	4aβ	>45	
		Middle	Elnes	4aα 3cd	ca. 60	
			Huk	3c	ca. 7	
		Lower	Tøyen	3b	ca. 20	
			Bjørkåsholm	3aγ	ca. 1	
	Cambrian	Upper — 485 Ma	Alum Shale	3a 2e	ca. 75	
		Middle				
		Lower — 541 Ma				

Figure 2: Stratigraphy of Lower Paleozoic in the central part of the Oslo Region with the thickness in metres. Simplified lithology shows Precambrian basement as vertical black/white streaks, shale as solid black, limestone as a brick pattern, and sandstone as dotted on a red/yellow background. Geological time and unit thickness are not to scale; time boundaries represent commonly accepted estimates. Figure modified after Nakrem and Worsley (2013).

2.2.3. Silurian

Silurian (444–419 Ma) units in the Oslo Region reach up to two kilometres in thickness. Early in the Silurian period, some northern areas remained above sea level, while areas around today's Bærum and Oslo subsided into deeper water environments where darker shales (Fig. 2; stage 8a-b) were deposited. The southwest and northwest areas were shallower, with near-shore deposits of sand and limestone. Continued subsidence in the northern areas of the Oslo Region produced relatively thick, sand-rich units with erosion material from the rising Caledonian mountains. In contrast, more central parts of the Oslo Region show a transition from shallow-water limestones, often containing thick shell beds and small reef structures, to deeper-water, darker limestones and shales.

Throughout the Late Ordovician and into the Silurian period, the areas that make up today's Scandinavia were compressed and deformed during the Caledonian orogeny (455–405 Ma), which caused Lower Paleozoic units in the Oslo Region to be folded and faulted. The deformation intensity increased northward toward Mjøsa. As mentioned, the orogeny generally caused significant folding, faulting, and metamorphism of Lower Paleozoic sedimentary rocks in western Scandinavia. In the Oslo Region, however, less deformation occurred because these units lay east of the main Caledonian thrust front. Later subsidence in the Permian Oslo Rift then shielded them from erosion (Nakrem and Worsley, 2013).

3. Why is the mineralogy of black shales important?

Lower Paleozoic black shales are widespread in Scandinavia (Fig. 3), and their mineralogical composition largely controls their chemical reactivity and physical properties. This chapter provides an overview of important geochemical and physical aspects of these fine-grained sedimentary rocks, as described in the literature.

In the Oslo Region, black shales such as the Alum Shale Formation are generally composed of quartz, feldspars, clay minerals (Bjørlykke, 1974), sulphides and minor amounts of carbonate minerals (the latter sometimes in the form of calcareous nodules; Pabst et al., 2016). In many shales, the clay concentration can be as high as 60%, accompanied by roughly 30% quartz/feldspar, and about 10% carbonates, plus trace mineral phases like iron oxides and sulphides (Rimstidt et al., 2017).Their deposition under prolonged anoxic conditions with extremely low sedimentation rates (about 1 mm per 1000 years; Bjørlykke, 1974), cause these shales to also contain relatively high concentrations of heavy metals (e.g. Cu, Ni, U, V), and organic matter (Pabst et al., 2016).
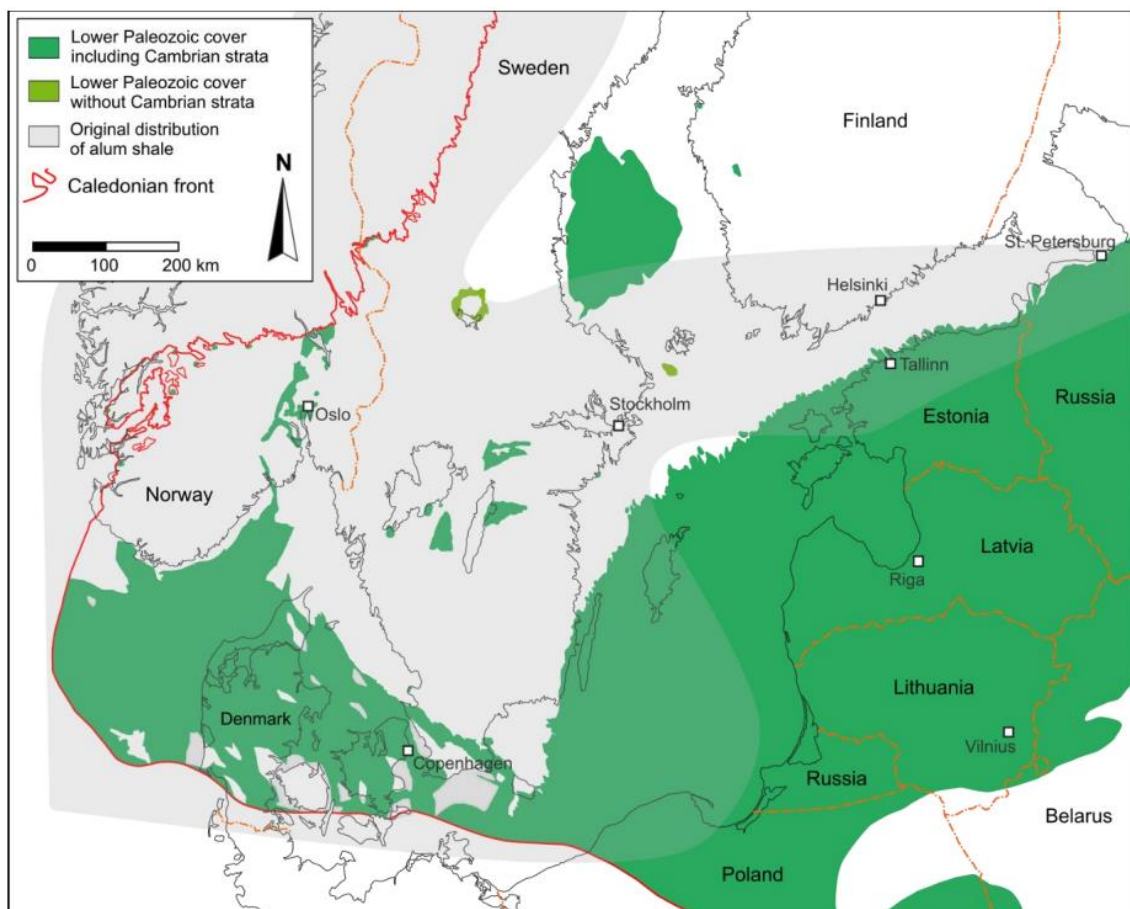
Figure 3: North European distribution of Cambrian sedimentary rocks, which includes the Alum Shale Formation. Map modified by Jan Marten Huizenga (unpublished) from Nielsen et al. (2018).

3.1 Acid rock drainage and acid potential

The sulphide minerals in black shales (primarily pyrite and pyrrhotite; Bjørlykke 1974, Pabst et al., 2016) can potentially generate acid rock drainage (ARD) when exposed to air and water–for example, through mining operations (in which case, it is called acid mine drainage), natural weathering, or construction activities (e.g., construction of roads and tunnels, residential property, etc.). The oxidation of sulphide minerals generates an acidic runoff, which can lead to acidification of surrounding ecosystems and mobilize toxic heavy metals into the environment (Dold, 2017).

3.1.1. Pyrite

Pyrite is the predominant sulphide mineral found in black shales (Bjørlykke, 1974). Its oxidation occurs in the presence of both oxygen and water, following the reaction (Dold, 2017):

$$FeS_2 + \frac{15}{4}O_2 + \frac{7}{2}H_2O \Rightarrow Fe(OH)_3 + 2SO_4^{2-} + 4H^+ \qquad (1)$$
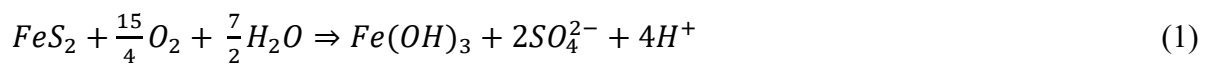
The reaction releases 4 moles of protons (H^+) for each mole of pyrite oxidized, contributing to the acidic conditions associated with ARD. The resulting acidity can increase solubility and mobility of heavy metals, such as cadmium, lead, and zinc, which can contaminate surface and groundwater resources (Dold, 2017).

Under specific conditions (e.g., at pH > 4 or by bacterial activity at pH < 4), ferrous iron (Fe^{2+}) produced in the primary reaction can further oxidize to ferric iron (Fe^{3+}) when exposed to oxygen (Dold, 2017):

$$Fe^{2+} + \frac{1}{4}O_2 + H^+ \Longleftrightarrow Fe^{3+} + \frac{1}{2}H_2O \qquad (2)$$

This reaction is proton-neutral, meaning it does not directly lower pH. However, when exposed to oxygen and water, the ferric iron (Fe^{3+}) can undergo hydrolysis to form ferric hydroxide ($Fe(OH)_3$), releasing 3 moles of protons (H^+) for each mole Fe^{3+} (Dold, 2017):

$$Fe^{3+} + 3H_2O \Leftrightarrow Fe(OH)_3 + 3H^+ \qquad (3)$$
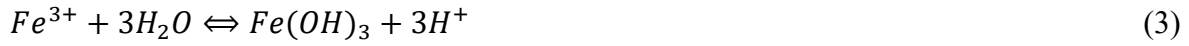
Ferric hydroxide can usually be observed as a reddish-brown precipitate in ARD-affected areas. Additionally, in more acidic environments (pH < 3.5), ferric iron (Fe^{3+}) remains in solution and acts as an oxidizing agent for pyrite (FeS_2) which can accelerate ARD (Dold, 2017):

$$FeS_2 + 14Fe^{3+} + 8H_2O \Rightarrow 15Fe^{2+} + 2SO_4^{2-} + 16H^+ \qquad (4)$$
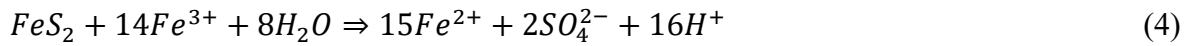
The total amount of acid liberating minerals and moles of protons that can potentially be liberated from a rock is commonly known as the rocks Acid Potential (AP; Dold, 2017). For black shales, early diagenesis is usually when pyrite formation starts below the sediment-water boundary, and when sediments get buried deeper, they experience higher temperatures which can further modify sulphide minerals and potentially make them react more easily when brought back up to the surface through geological processes (Rimstidt et al., 2017).

3.1.2. Pyrrhotite

Pyrrhotite ($Fe_{(1-x)}S$), a secondary sulphide mineral in black shales, has also been identified in black shales of the Oslo region (Bjørlykke, 1974). Pyrrhotite is presumed to have formed through low-grade metamorphism associated with the Caledonian orogeny, which facilitated the transformation of some pyrite into pyrrhotite, but this has historically not been considered a primary sulphide mineral in these shales (Bastiansen et al., 1957). Still, pyrrhotite may oxidize at similar, or even faster rates than pyrite (Gleisner and Herbert Jr., 2002; Janzen et al., 2000; Table 1). This means that even minor quantities of pyrrhotite, where present in these shales, can play a significant role in driving the generation of ARD (Dold, 2017).

Table 1: Experimental oxidation rates including uncertainties for the sulphide minerals pyrite and pyrrhotite at pH = 2-3. Rates are based on oxidation via ferric iron (Fe^{3+}) and given in units of moles per square meter (m^2) per second (s). The table also includes amounts of protons (H+) liberated per mole of mineral oxidized (Data compiled and modified after Dold, 2017; Gleisner and Herbert Jr., 2002; Janzen et al., 2000).

Sulphide mineral	Oxidation rate (mol/m²/s)	Mol H+ per mol sulphide
Pyrite	$5.59 \, (\pm 1.59) \times 10^{-11}$	16 mol (eq. 4)
Pyrrhotite	$4 \, (\pm 6) \times 10^{-9}$	8 mol (eq. 6)

Similarly to pyrite, pyrrhotite undergoes oxidation in the presence of oxygen and water, releasing ferrous iron (Fe^{2+}), sulphate (SO_4^{2-}), and protons (H^+) that contribute to acidification which can increase ARD through the following reaction (Dold, 2017; Nicholson and Scharer, 1994):

$$Fe_{1-x}S + \left(2 - \frac{1}{2}x\right)O_2 + xH_2O \Rightarrow (1-x)Fe^{2+} + SO_4^{2-} + 2xH^+ \tag{5}$$
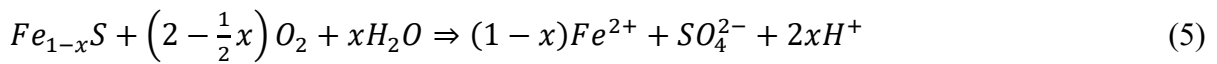
Under acidic conditions, ferric iron (Fe^{3+}) can reach high concentrations and as previously mentioned (Equation 4) also serve as an oxidizing agent, releasing additional ferrous iron (Fe^{2+}), sulphate (SO_4^{2-}), and acidity (H^+) into the water. For pyrrhotite the reaction can be written as (Nicholson and Scharer, 1994):

$$Fe_{1-x}S + (8 - 2x)Fe^{3+} + 4H_2O \Rightarrow (9 - 3x)Fe^{2+} + SO_4^{2-} + 8H^+ \tag{6}$$
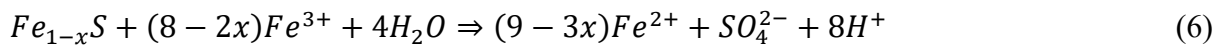
3.2. Acid Neutralizing Potential

The ARD produced from sulphide mineral oxidation in black shales can be partially or fully neutralized by other mineral groups present within the rock or adjacent areas through dissolution and weathering processes. The most significant contributors to acid neutralization are carbonate minerals, hydroxides, and the silicate minerals. The ability of a rock to neutralize acidity is quantified as its Neutralization Potential (NP). Together with the rock's AP, these values determine whether the system is acid-producing or acid-neutralizing. If NP exceeds AP, the rock is considered acid-neutralizing. Otherwise, it may contribute to ARD when exposed to water and oxygen (Dold, 2017).

3.2.1. Carbonate minerals

Calcite ($CaCO_3$) and dolomite ($CaMg(CO_3)_2$) are among the most effective acid-neutralizing minerals due to their relatively quicker dissolution (Table 2). The intermediate neutralizing reaction for calcite (Dold, 2017):

$$CaCO_3 + H^+ \Rightarrow Ca^{2+} + HCO_3^- \qquad (7)$$

This reaction buffers the acidity and helps stabilize pH through the dissolution of calcite. Dolomite is not usually found directly in Alum shale, but it is considered as one of the most prevalent minerals in adjacent Lower Palaeozoic stratigraphy (for example, in limestone; Bjørlykke, 1974). Dolomite reacts similarly to calcite but more slowly (Dold 2017), contributing to longer-term neutralization as it gets dissolved, through the following reaction (Gomo, 2018):

$$CaMg(CO_3)_2 + 2\,H^+ \Rightarrow Ca^{2+} + Mg^{2+} + 2\,HCO_3^- \qquad (8)$$
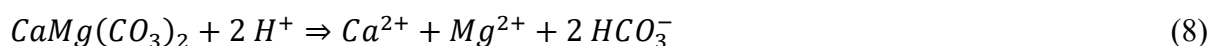
The buffering effect of carbonate minerals can maintain pH levels in a neutral to slightly alkaline range as long as these minerals are present in sufficient quantities (Dold, 2017). However, it is important to note that the presence of carbonate minerals does not entirely prevent the release of heavy metals into the environment. If sulphide minerals continue to oxidize, even under near-neutral or slightly alkaline conditions, certain alum shale heavy metals (e.g., Cd, Ni, Mn, U) can remain mobile in solution (Pelkonen et al., 2025).

Table 2: Relative reactivity in acid-neutralization capacity of minerals (after Dold, 2017; Sverdrup, 1990). Modified to highlighting acid neutralizing minerals found in black shales (Bjørlykke, 1974).

Reaction/process	Typical minerals	Relative reactivity (pH = 5)
Dissolution	Calcite, dolomite	1.0
Intermediate weathering	Chlorite	0.4
Slow weathering	Plagioclase, kaolinite	0.02
Very slow weathering	K-feldspar, muscovite	0.01
"Inert"	Quartz, rutile, zircon	0.004

inert is used relatively to geochemical processes involving the other minerals shown, as no mineral is completely immune to weathering (Dold, 2017).

3.2.2. Hydroxide minerals

Hydroxide minerals can both increase and mitigate ARD. Their formation, for example through the hydrolysis of ferric iron (Fe^{3+}) shown in Equation 3 releases protons, contributes to acidity. However, ferric hydroxides also act as buffers in acidic environments (pH values of 3.0–4.0) by dissolving and consuming protons, helping to stabilize pH in this range. At higher pH levels (pH > 3.5), ferric hydroxide precipitates, which removes Fe^{3+} from solution. This reduces the availability of Fe^{3+} to oxidize sulphide minerals, indirectly lowering the overall AP capacity of the system, as oxidation is the primary driver of acid production (Dold, 2017).

3.2.3. Silicate minerals

Silicate minerals, including feldspars, clays, and micas, play a minor role in acid neutralization due to their relatively slow weathering rates (Table 2). Although far less reactive than carbonates and hydroxides, their weathering gradually releases cations such as calcium, magnesium, and sodium, providing long-term buffering (Dold, 2017). In black shales, where these silicate minerals are the main constituents (Bjørlykke, 1974), this process provides a gradual but persistent contribution to acid neutralization over geological timescales (Dold, 2017).

On the other hand, as these weathering processes occur on longer timescales (Table 2) post-depositional changes of clay minerals (e.g., smectite converting to illite) and feldspars (e.g., albitization) can mobilize elements such as iron, manganese, zinc, and lead into pore waters. These processes continue until the shales are exposed to low-grade metamorphism. Once exhumed, renewed weathering and oxidation can liberate additional elements, including heavy metals, if local acid-neutralizing capacity is insufficient (Rimstidt et al., 2017).

3.3. Brittleness and hydraulic conductivity

Mineralogy is also a main factor in determining the mechanical properties of shales, especially their brittleness (Bailey et al., 2022). This influences the rock's potential to develop fractures which affects its hydraulic conductivity (Zimmerman and Bodvarsson, 1996). Brittleness describes how likely a rock is to fracture under stress with limited plastic

deformation. In contrast, ductility describes its ability to deform plastically ("flow") before fracturing (Bailey et al., 2022).

This behaviour is mainly influenced by the proportion of harder minerals such as quartz, carbonates and feldspars versus the amount of softer minerals like the clay minerals. For example, high quartz content enhances brittleness due to its resistance to plastic deformation, while minerals like smectite or illite, that contain structural water, increase ductility and reduce brittleness (Bailey et al., 2022; Rimstidt et al., 2017).

Because a more brittle shale will break more easily under stress, it also has a higher chance of developing interconnected fractures than a more ductile shale. While the rock itself can have low permeability, these fractures greatly increase the bulk hydraulic conductivity of areas that have higher ratios of brittle versus ductile minerals (Rimstidt et al., 2017; Zimmerman and Bodvarsson, 1996).

Hydraulic conductivity quantifies the ease with which fluids, primarily water in this context, can flow through the rock matrix (Zimmerman and Bodvarsson, 1996). In the context of ARD this becomes important because a rock mass with greater hydraulic conductivity will get more exposure to oxygenated water, meaning more sulphide mineral surfaces (e.g., pyrite) can come into contact with O_2 and H_2O. If a more fractured, brittle shale gets exposed to surface water (e.g., during construction work) it can also potentially facilitate greater transport of runoff water, and therefore increase the overall risk or rate of ARD (Dold, 2017; Zimmerman and Bodvarsson, 1996).

4. Overview of mineral identification and quantification methods

Mineral identification and quantification typically involve analytical methods that determine one or more of the following: (1) the types and proportions of mineral phases present, (2) their chemical compositions and compositional variations, and (3) the structural characteristics of individual mineral grains.

Conventional methods rely on observing the optical properties of minerals (e.g. colour, birefringence, extinction angle, etc.) via microscopy using thin sections, but these methods are limited, especially in fine-grained samples (e.g. shales), where magnification limits and the complex distribution of mineral grains make identification and quantification more difficult. Also, microscopic identification of minerals is a highly specialized skill.

Over time, modern methods utilizing X-ray or electron-emitters have emerged to address the increased demand for detailed mineralogical data (environmental science, mining industry, etc.). The theory behind these newer methods have been discussed comprehensively in the literature, for example by Lou et al. (2020). This chapter provides an overview of the most common methods of mineralogical analysis used today.

4.1. X-Ray Diffraction

X-ray diffraction (XRD) analyses the crystalline properties of minerals to identify mineral phases within a sample (Lou et al., 2020). In this method, beams of X-rays directed at a crystalline substance scatter in a pattern controlled by Bragg's law, which relates diffraction angles (meaning the change in direction when the beam enters a new medium) to the spacing of crystal planes. Each mineral has a characteristic atomic arrangement that produces a unique pattern of diffraction peaks. The positions of these peaks help identify the mineral by matching them to reference data, while the intensities are proportional to the mineral's abundance in the sample. (Lou et al., 2020). This method can reveal small differences among minerals, such as various polymorphic forms of silicates, carbonates, or titanium oxides (Lou et al., 2020).

However, XRD has a relatively high detection limit causing some level of uncertainty (±5.2 wt.%; Hillier, 2000) meaning minerals present in small quantities may be overlooked (Lou et al., 2020). Also, the beam itself only penetrates some tens of micrometres into most dense materials (like minerals), so direct XRD analysis is mostly sensitive to near-surface regions

of a sample (Epp, 2016). The analysis takes slightly longer than other methods, with complete scanning of samples requiring at least 10 minutes, but scan times can be upwards of an hour depending on instrument configuration and resolution demands (Epp, 2016; Khan et al., 2019). For full quantitative analysis, sample preparation usually includes grinding the rock into a fine powder (Lou et al., 2020), a step that contributes additional time and cost to this method. According to the current ALS Geochemistry Fee Schedule (ALS is a laboratory commonly employed for chemical analysis in Norway), typical baseline cost of a fully quantitative XRD analysis is approximately 400 USD per sample (ALS, 2025).

4.2. Scanning Electron Microscopy and Automated Mineralogy

Scanning electron microscopy (SEM) generates detailed images of a sample's surface by scanning each tiny section with an electron beam. Most SEM instruments are combined with an energy dispersive X-ray (EDX) detector for quantitative elemental analysis (Lou et al., 2020) Various signals, including secondary electrons and backscattered electrons, emerge when the beam interacts with the sample's surface. Secondary electron imaging emphasizes surface features, while backscattered electron imaging highlights compositional contrasts related to atomic number differences (Lou et al., 2020).

Automated mineralogy (AM) systems integrate SEM instruments with specialized computer software, together with EDX detectors and automated precise sample preparation. Examples of such systems include QEMSCAN and TIMA (Lou et al., 2020). These configurations systematically acquire SEM-data, and corresponding EDX-data of sample surfaces, and then digitally classifies each pixel or defined segment by matching its composition against a database of known minerals (Lou et al., 2020). Despite a high level of automation, these methods require trained personnel to oversee and operate the equipment (Rollinson et al., 2011), making SEM and AM systems among the more expensive, but overall most precise options for mineralogical analysis.

4.3. Electron Probe Microanalysis

Electron probe microanalysis (EPMA) is another commonly used technique for obtaining high-resolution elemental data from solid samples, but it does not directly identify minerals. Instead, mineralogical interpretation relies on combining elemental data with textural features

and/or supporting methods like XRD (Goodge, 2018; Pownceby et al., 2007). Like SEM-based systems, EPMA detects X-rays emitted from a sample exposed to an electron beam, with the energies of the X-rays corresponding to specific elements. This technique provides both qualitative and quantitative data at the micrometre scale (Goodge, 2018).

EPMA systems are equipped with wavelength dispersive (WD) and energy dispersive (ED) spectrometers to detect the emitted X-rays, offering even better precision than SEM-EDX (Goodge, 2018). Wavelength dispersive spectrometers can separate overlapping X-ray peaks, which is necessary for analysing minerals containing elements with similar X-ray signals, such as rare-earth minerals (Pownceby et al., 2007). Analytical precision is typically better than 2% for major elements and elemental concentrations can be measured within microscopic volumes (Goodge, 2018). However, EPMA cannot detect the lightest elements (e.g., hydrogen) resulting in the inability to analyse the water content in hydrous minerals (Goodge, 2018).

By collecting X-ray elemental distribution, backscattered electron (BSE), and cathodoluminescence (CL) data, direct correlations between chemical composition and textural features within a sample can be made. This capability helps to identify minerals with similar chemical composition and detecting trace elements (Pownceby et al., 2007). Output data include elemental maps, scatter plots, and ternary diagrams to visualize the distribution of minerals and their chemical differences (Pownceby et al., 2007). Accurate EPMA results rely on thorough sample preparation, including the creation of finely polished surfaces and the application of a conductive coating to mitigate charging effects caused by the electron-beam during analysis (Goodge, 2018). Specialized skills are also required to process and interpret output data, making EPMA systems among the more expensive, but accurate methods used related to mineralogical analysis.

4.4. Raman spectroscopy

Raman spectroscopy (RS) uses a process called Raman scattering (Raman and Krishnan, 1928), where intense light interacts with molecules in a sample, causing the light's energy to shift. In this process, the incoming light temporarily excites the molecule, and as it then returns to its original state, the molecule emits light at a slightly different frequency. These differences, known as Raman shifts, are unique to the molecules in a sample (Rostron et al., 2016). By measuring these shifts, it is possible to identify various materials, including

minerals. Samples can be measured directly and require not more than a few minutes, and the technique is non-destructive, which prevents contamination of the sample and limits the need for extensive sample preparations (Lou et al., 2020; Rostron et al., 2016).

Interestingly, a spectrometer of this kind is one of the instruments onboard NASA's Perseverance Rover, which is actively exploring Mars' surface and conducting mineralogical studies, among other investigations (Bhartia et al., 2021).

There is relatively little literature describing its use for large-scale mineral quantification, though it has been applied for example in assessing shales maturity for the petroleum industry (Sauerer et al., 2017). Nonetheless, this method is portable, (very) fast, and affordable (e.g., Rostron et al., 2016).

4.5. X-ray fluorescence

X-ray fluorescence (XRF) identifies the chemical composition (major elements and trace elements) of a sample (Secchi et al., 2018) by measuring the secondary (fluorescent) X-rays emitted from a sample that has been excited by an incoming high-energy X-ray beam (Lou et al., 2020). When the incoming X-ray beam knocks out electrons from an inner atomic shell in the sample, electrons from higher energy levels fill these vacancies, releasing X-ray photons at energies unique to each element. The positions and intensities of the resulting X-ray emission lines are directly related to the types and quantities of elements present in the sample (Lou et al., 2020).

X-ray fluorescence can quantify elements all the way down to a few parts per million (ppm), is typically completed in under five minutes per sample (Lou et al., 2020), and it is in general considered the most common method used for chemical analysis of rocks (Oyedotun, 2018). However, optimal results require that the sample be pulverized into a powder and then either pressed or fused into a disc, which requires additional time for sample preparation. Whole rock XRF analysis costs approximately 40 USD per sample (ALS, 2025)–placing it among the cheaper analysis methods.

This method does not directly give mineralogical information (Lou et al., 2020). However, the analysis data does allow the indirect determination of the mineralogy in two ways. First, the major element composition can be used to calculate the mineral content, referred to as CIPW norm method, named after the petrologists Charles Cross, Joseph Iddings, Louis

Pirsson, and the geochemist Henry Washington who developed this method (Cross et al., 1902; Wagner et al., 2020). CIPW was initially developed for igneous rocks but has been modified for other rock types like shale and will be explained in more detail in the next chapter. Second, certain trace element concentrations may be an indicator for the presence of specific minerals, for example, As can be related to pyrite, and Ba can be related to barite (Cross et al., 1902).

4.6. Artificial intelligence

Recent artificial intelligence (AI) advances have applied convolutional neural networks (CNNs) to image-based mineral identification. These networks automatically extract features from digital images, reducing human error in defining mineral characteristics. Using an approach similar to face recognition, CNNs capture subtle variations in texture, colour, and other visual properties–much like optical microscopy before it. However, they remain emerging technologies that require further development for large-scale use (Lou et al., 2020).

5. Methodology used in this study

This chapter describes the software tool *SlateNorm*, which was used in this study, attempting to determine and quantify shale mineralogy based on normative mineral calculations. Mineralogical quantification of fine-grained rocks (slates, shales, phyllites) previously carried out using this software (Wagner et al., 2020), provides the foundation for discussing the practicality of applying SlateNorm in the manner described in this study. Methods used to assess SlateNorm outputs are also described in this chapter.

5.1. SlateNorm software

SlateNorm, which was published by Wagner et al. (2020), was initially designed to assess mineralogical suitability of slate for roofing purposes (Wagner et al., 2020). SlateNorm is implemented as software tool, and the calculations follows a step-by-step algorithm outlined in section 5.1.2. (Appendix C; Wagner et al., 2020). The software generates grouped mineral outputs, including feldspars, carbonates, micas, chlorites, ore-minerals, and the minerals quartz, chlorite, pyrite, graphite and apatite (Wagner et al., 2020).

In the software (Fig. 4) oxide compositions from chemical analyses (typically obtained from XRF data) are converted into molecular numbers by dividing each oxide's concentration by its molecular weight (Wagner et al., 2020). These sums are then used to calculate normative minerals, each defined by a specific chemical composition, thereby providing a theoretical estimate of the rock's mineralogy (Wagner et al., 2020).

	Sample	Sym	Wid	Col	il/ru	SiO2	TiO2	Al2O3	Fe2O3	FeO	MnO	MgO	CaO	Na2O	K2O	P2O5	C(org)	CO2	H2O+	S	Sum
1	Geochemical input					9.00	0.60	11.15	0.00	4.28	0.03	1.22	0.74	0.10	6.41	0.11	9.27	0.00	0.00	3.03	85.94
2						0.20	0.64	11.65	0.00	3.59	0.02	1.03	0.23	0.06	6.73	0.04	9.30	0.00	0.00	2.39	85.88
3	3	2	6	1	0	48.40	0.61	11.40	0.00	3.95	0.02	0.98	0.22	0.06	6.62	0.08	9.92	0.00	0.00	2.81	85.07
4	4	2	6	1	0	47.40	0.61	11.35	0.00	3.74	0.02	0.98	0.19	0.05	6.53	0.06	11.15	0.00	0.00	2.72	84.80
5	5	2	6	1	0	47.30	0.62	11.50	0.00	3.96	0.02	0.98	0.22	0.06	6.71	0.09	11.15	0.00	0.00	3.01	85.62
6	6	2	6	1	0	46.60	0.61	11.10	0.00	5.22	0.02	0.92	0.23	0.07	6.48	0.09	8.24	0.00	0.00	4.46	84.04
7	7	2	6	1	0	48.30	0.65	11.75	0.00	4.12	0.02	1.03	0.23	0.06	6.76	0.13	8.46	0.00	0.00	2.85	84.36
8	8	2	6	1	0	47.10	0.64	11.60	0.00	3.93	0.02	1.00	0.18	0.05	6.67	0.05	9.90	0.00	0.00	2.78	83.92
9	9	2	6	1	0	44.60	0.64	11.70	0.00	3.97	0.02	1.07	0.17	0.07	6.63	0.04	11.50	0.00	0.00	2.91	83.32
10	10	2	6	1	0	48.90	0.66	12.00	0.00	4.28	0.02	1.01	0.18	0.10	6.91	0.05	8.91	0.00	0.00	2.89	85.91
11	11	2	6	1	0	46.60	0.66	11.95	0.00	4.03	0.02	1.02	0.17	0.10	6.89	0.03	10.85	0.00	0.00	2.98	85.30

Figure 4: *Screenshot of SlateNorm software showing imported geochemical data in wt.% (below red headers) output window follows on next page (see Fig. 4 continued).*

qz	mu	pa	or	ab	an	mac	fac	mc	fc	ct	cc	dol	sid	pt	gr	ilm	ru	ap	aq	sum
Calculated mineralogy					3.42	0.00	0.00	3.24	1.83	0.00	0.00	0.00	0.00	6.58	10.75	0.00	0.70	0.30	0.00	100.00
23.04	17.05	0.00	33.55	0.55	1.02	0.00	0.00	2.73	1.86	0.00	0.00	0.00	0.00	5.17	10.76	0.00	0.74	0.11	0.00	100.00
24.60	17.95	0.00	33.22	0.59	0.67	0.00	0.00	2.63	1.66	0.00	0.00	0.00	0.00	6.15	11.60	0.00	0.71	0.22	0.00	100.00
24.06	18.32	0.00	32.47	0.50	0.65	0.00	0.00	2.64	1.44	0.00	0.00	0.00	0.00	5.97	13.08	0.00	0.72	0.16	0.00	100.00
22.96	17.97	0.00	33.57	0.59	0.59	0.00	0.00	2.61	1.22	0.00	0.00	0.00	0.00	6.55	12.97	0.00	0.72	0.24	0.00	100.00
23.96	17.55	0.00	33.38	0.71	0.66	0.00	0.00	2.51	0.50	0.00	0.00	0.00	0.00	9.95	9.82	0.00	0.73	0.25	0.00	100.00
24.04	19.46	0.00	33.48	0.60	0.34	0.00	0.00	2.78	1.92	0.00	0.00	0.00	0.00	6.28	9.97	0.00	0.77	0.36	0.00	100.00
23.20	18.94	0.00	33.48	0.50	0.67	0.00	0.00	2.72	1.71	0.00	0.00	0.00	0.00	6.16	11.73	0.00	0.76	0.14	0.00	100.00
20.40	19.56	0.00	33.10	0.71	0.69	0.00	0.00	2.93	1.50	0.00	0.00	0.00	0.00	6.50	13.73	0.00	0.76	0.11	0.00	100.00
23.18	18.76	0.00	34.15	0.98	0.66	0.00	0.00	2.68	2.12	0.00	0.00	0.00	0.00	6.26	10.31	0.00	0.76	0.13	0.00	100.00
20.95	18.65	0.00	34.48	0.99	0.76	0.00	0.00	2.73	1.43	0.00	0.00	0.00	0.00	6.51	12.66	0.00	0.77	0.08	0.00	100.00

Figure 4: *(continued) calculated mineralogy in wt.% (below blue headers). Note that calculated mineralogy (outputs) appears on the same row when using the software, immediately left of inputs; it is shown below here to fit the page.*

5.1.1. Data requirements and output mineralogy

The software requires precise input of major element oxide compositions and specific volatile components (Table 3) to calculate theoretical mineral compositions (Table 4; Table 5). The output minerals represent grouped normative minerals defined by specific chemical compositions (Table 5; Wagner et al., 2020).

Table 3: Required input data for normative mineral calculations in SlateNorm.

Major Oxides	SiO_2, TiO_2, Al_2O_3, Fe_2O_3, FeO, MnO, MgO, CaO, Na_2O, K_2O, P_2O_5
C, S and $(H_2O^+)^*$	CO_2, organic C, elemental S, structural water content

$(H_2O^+)^*$: is included as an input in the software; however, this value will not affect the calculated mineralogy

In the documentation, it is noted that accuracy of the calculations depends on differentiating carbonate from non-carbonate C, and defining S as elemental S rather than SO_3 (Wagner et al., 2020).

Table 4: Output mineralogy as calculated by SlateNorm, with minerals/mineral groups following Wagner et al. (2020).

Mineral group	Abbrivation	Mineral name
Feldspars	an, ab, or	Anorthite, Albite, Orthoclase
Carbonates	cc, dol, sid	Calcite, Dolomite, Siderite
Micas/Clay	mu, pa	Muskovite, Paragonite
Chlorites	mac, fac, mc, fc	Amesite, Dapnite, Serpentine, Greenalite
Sulphides	pt	Pyrite
Other minerals	qz, ct, gr, ilm, ru, ap, (aq*)	Quartz, Chloritoid, Graphite, Ilmenite, Rutile, Apatite, H_2O (residual water)

aq*: H_2O is included as residual water; however, this value will always be output as zero regardless of input data. Mineral abbreviations are explained in Table 5.

21

Table 5: Minerals in SlateNorm and corresponding mineral chemistry (after standard CIPW norm; Wagner, 2022).

Mineral name	Mineral chemistry
Anorthite (an)	$CaO \cdot Al_2O_3 \cdot 2SiO_2$
Albite (ab)	$Na_2O \cdot Al_2O_3 \cdot 6SiO_2$
Orthoclase (or)	$K_2O \cdot Al_2O_3 \cdot 6SiO_2$
Calcite (cc)	$CaO \cdot CO_2$
Dolomite (dol)	$CaMg(CO_3)_2$
Siderite (sid)	$FeCO_3$
Muskovite (mu)	$KAl_2(AlSi_3O_{10})(OH)_2$
Paragonite (pa)	$NaAl_2(AlSi_3O_{10})(OH)_2$
Amesite (mac)	$Mg_2Al(AlSiO_5)(OH)_4$
Dapnite (fac)	$(Fe^{2+},Mg)_3(Fe^{3+},Al)_2(Si,Al)_4O_{10}(OH)_8$
Serpentine (mc)	$(Mg,Fe)_3Si_2O_5(OH)_4$
Greenalite (fc)	$(Fe^{2+})_{2-3}Si_2O_5(OH)_4$
Pyrite (pt)	FeS_2
Quartz (qz)	SiO_2
Chloritoid (ct)	$(Fe,Mg,Mn)_2Al_4Si_2O_{10}(OH)_4$
Graphite (gr)	C
Ilmenite (ilm)	$FeTiO_3$
Rutile (ru)	TiO_2
Apatite (ap)	$Ca_5(PO_4)_3(F,Cl,OH)$

5.1.2. Overview of steps in algorithm

The mineralogical and geochemical principles underlying the SlateNorm algorithm are relatively complex. For a more in-depth overview of the algorithm, the reader is referred to Appendix C. A simplified overview of the calculation steps performed by SlateNorm is provided below.

Steps in SlateNorm algorithm:

1. Calculation of apatite from P_2O_5.

2. Calculation of sulphides (primarily pyrite) from S.

3. Determination of Ti-bearing minerals, including ilmenite and rutile.

4. Carbonate mineral calculations (calcite, dolomite, siderite) using CO_2 content.

5. Calculation of feldspars from CaO, Na$_2$O, and K$_2$O.

6. Determination of micas (muscovite, paragonite).

7. Chlorite group calculations, distinguishing Fe-chlorites (daphnite, greenalite) and Mg-chlorites (amesite, serpentine).

8. Calculation of quartz and other residual minerals (chloritoid, graphite) from remaining oxides (Wagner, 2022).

5.1.3. Utility and known limitations

The SlateNorm software provides a systematic and reproducible means of estimating mineralogy, developed to overcome some of the inherent challenges associated with direct petrographic observations of fine-grained sedimentary rocks (Wagner et al., 2020). However, initial testing of SlateNorm in this project revealed certain limitations: although the software accepts H$_2$O$^+$ as an input, it does not currently incorporate this water properly into the mineralogical calculations (i.e., the results are the same regardless of whether H$_2$O$^+$ is included or not). In short, this means that the normative mineralogy calculated by SlateNorm may not fully reflect actual sample compositions, especially for minerals that structurally contain H$_2$O$^+$ (OH$^-$ groups; see Table 5). Furthermore, SlateNorm is only able to assign sulphur to pyrite, it does not include pyrrhotite in its calculations or outputs.

Finally, SlateNorm remained unpublished software until 2020, and so there is limited practical documentation, such as a manual or user guide. The software shows signs typical of early-stage or older software, including: an unintuitive user interface, lack of labelled buttons or clear error messages, and is prone to crashing/shutting down when encountering unexpected inputs.

5.1.4. Practical workflow in Slatenorm

This chapter outlines the general workflow in SlateNorm as it was discovered through practical use during this study. The steps described here are based on trial and error and hands-on experience.

Data formatting for SlateNorm input

The first step is compiling the required sample data outlined in section 5.1.1. Although it is possible to manually enter each parameter (oxide, element etc.) for each sample directly into SlateNorm, a more practical method is to import pre-formatted files containing all required geochemical data at once. Upon importing data, SlateNorm presents several input format options, including "NewPet" or "IgPet" data, which are file formats used in igneous petrology (Carr and Gazel, 2017). These files, with a ".roc" file extension can be created and edited using standard text editors such as Notepad++.

In this project, the "IgPet data (tab-delimited)" format was exclusively used due to its readability and ease of manual editing. Data must match the IgPet format exactly, as any deviation may cause errors or force the software to close unexpectedly. The data files formatted according to these requirements used in this project are provided in Appendix D.

Manual data conversion from tables in papers to the required input format is time-consuming. As such, partial automation of this step was performed using artificial intelligence (AI) by prompting freely available (as of year 2025) Large Language Models (LLMs), specifically ChatGPT (OpenAI) and DeepSeek (DeepSeek AI). To ensure accurate data handling, clear examples of both input and expected output were provided to the LLMs, and model outputs were manually verified to avoid errors.

Importing Data into SlateNorm

Unlike modern software that supports intuitive file handling methods like drag-and-drop, SlateNorm requires the user to follow specific steps for data import. After creating a correctly formatted input file, import can only be done by selecting "File," then "Import," choosing the "IgPet data (tab-delimited)" option, and selecting the input file. Additionally, it is critical to ensure that the numerical data (chemical composition of samples) use a period (.) as a decimal separator, since commas (,) are not recognized by SlateNorm and will result in import errors.

Running calculations and exporting results

Running the calculation is simple and instant; users must press the F2 key or select the "Norm" button followed by the "Basic version" option from the pop-up window, which is the

version recommended by Wagner et al. (2020). The resulting mineralogical data will be displayed within the software window. Users can export these results either directly as an IgPet file, now including the calculated mineralogy, or alternatively as an ASCII text file for subsequent analysis.

5.2. Comparative assessment

This section describes the methods used to compare and visualize SlateNorm-calculated mineralogy against reference XRD mineralogy across sample sets. Three approaches were used: (1) bar charts with absolute relative difference (%) between methods; (2) Lin's concordance correlation coefficient (r_c) plots with 95% confidence intervals (CI); and (3) a plot of the absolute relative difference against XRD-determined mineral quantities, following Casetou-Gustafson et al. (2018). Unless otherwise stated, all data were plotted and visualized using Excel.

Some sample pairs were excluded from comparisons due to large discrepancies between SlateNorm- and XRD-determined mineral concentrations or if SlateNorm output was negative (e.g., quartz = -10 wt.%). This exclusion also applied if mineralogy was not quantified by XRD in general (in other words, whenever mineralogy was only reported as trace amounts, or not at all, in XRD results). Exclusion was done based on case-by-case judgment, as a single rule could not be applied across data with different value ranges (i.e., minerals with relatively low or very high concentrations). Additionally, samples where SlateNorm calculated 0 wt.% were excluded, as this would yield a fixed 100% relative error, making them not provide meaningful information about SlateNorm's performance. The full data including outliers and excluded charts can be found in Appendix A and Appendix B respectively.

5.2.1. Absolute relative difference

The difference between SlateNorm and XRD mineral quantities as normalised weight percentage (wt.%) was expressed as an absolute percentage, treating under- and over-estimates the same, to show the magnitude of deviation of individual mineral quantities between methods within each dataset, and was calculated using the standard formula:

$$Absolute\ relative\ difference\ (\%) = \left|\frac{XRD_{wt\%} - SlateNorm_{wt\%}}{XRD_{wt\%}}\right| \times 100$$

5.2.2. Lin's Concordance Correlation Coefficient

Lin's concordance correlation coefficient (Lin's CCC; = r_c) was used to compare how well estimates/calculations from an experimental method (SlateNorm) matches an already established method (here: XRD; Lin, 1989). In this study, all calculations were carried out using an Excel template requiring an Excel add-on package (Real Statistics Resource Pack) to function, both of which are provided by Zaiontz (2025) on the Real-Statistics website. The spreadsheet uses an altered version of the original Lin's CCC formula to calculate the correlation coefficient (Lin, 1989; Zaiontz, 2025) and is expressed as:

$$r_c = \frac{2rs_x s_y}{(\overline{x} - \overline{y})^2 + s_x^2 + s_y^2}$$

where *r* is the Pearson correlation between the paired values (XRD and SlateNorm mineral wt.% respectively), $\overline{x}$ and $\overline{y}$ are their sample means, s_x and s_y are the population standard deviations calculated with denominator *n*, and *n* is the number of paired observations. A perfect result would yield r_c=1, whereas poor correlations would be closer to zero (Lin, 1989; McBride, 2005; Zaiontz, 2025). For further details and mathematical definitions of variables the reader is referred to Lin (1989) and McBride (2005). The Excel template also provides ninety-five-percent confidence intervals (95% CI), as described by Lin (1989), which were also included in the final plots.

Mcbride (2005) suggests interpreting Lin's r_c values >0.9 as a good correlation between compared values. However, due to SlateNorm's limitations discussed in chapter 5.1., it was decided that a more lenient r_c of >0.7 would be sufficient for the purpose of this study.

5.2.3. Absolute relative difference vs. XRD mineral quantities

The absolute relative difference percentage between XRD and SlateNorm mineralogy results (|XRD – SlateNorm|)/ XRD × 100), combining all datasets, was visualized in a scatterplot, plotted against XRD wt.% of the same minerals. This method of visualization follows a study

in which XRD soil mineral diffraction patterns were compared with modelled, indirect normative diffraction patterns (Casetou-Gustafson et al., 2018).

In their study, the full dataset scatterplot included a 95% confidence "error threshold" line, expressed as $\pm100X^{-0.65}$ which was determined by Hillier (2003). It visualizes that minerals present in lower quantities are usually harder to quantify due to detection limits and equipment tolerances (as highlighted in Chapter 4.1) inherent to XRD mineral analysis (Hillier 2003).

Points falling above the line indicates a deviation of the modelled method greater than precision expected of quantitative XRD analysis. Essentially meaning that any modelled results plotting above the error threshold can be considered to not have achieved sufficient accuracy (Casetou-Gustafson et al., 2018; Hillier, 2003).

It was determined that applying Hillier's threshold unchanged would judge SlateNorm, which comes with some inherent limitations (e.g., conditions in the underlying algorithm, previously mentioned ignored H_2O^+, and for the purpose of this study; required input data conversions), by a standard it can never match when tested on shale samples used in this study. To provide a fairer comparison that still highlights large deviations between each method across all mineral quantities, the original 95% CI was increased by a factor of two ($\pm100X^{-0.65} \rightarrow \pm200X^{-0.65}$). Meaning the 95% CI was converted to a general threshold more appropriate for this study, but still based on the same logical criteria.

Declaration: Use of AI writing tools

In line with university guidelines at NMBU, AI-based programs were used as a writing tool during the preparation of this thesis. Specifically, the LLMs ChatGPT (OpenAI) and Gemini (Google) were used to help with the writing process. This involved using these models to improve structure and conciseness of the text. All AI outputs were manually reviewed and edited to ensure accuracy and maintain the originally intended meaning and arguments.

6. Description and modification of geochemical data

Comprehensive datasets containing both complete whole-rock compositions and quantitative XRD results of shales are scarce in the literature. During the data collection process, several potential datasets had to be discarded because critical calculation parameters such as total sulphur and/or TOC were missing from the reported geochemical data in their respective papers.

In total, appropriate analytic data was compiled from four datasets (Appendix A), totalling 150 samples, which include major oxides determined by XRF, TOC and S determined by standard combustion elemental analysis methods, and mineralogy determined mainly by XRD. Full analytical procedures are described in the original, publicly available papers as cited below.

6.1. Datasets used in this study

Dataset 1: Cambro-Ordovician Khabour Formation, Iraq - Al-Juboury et al. (2020)

The first dataset consists of 15 shale core samples from the Cambro-Ordovician (539–444 Ma) Khabour Formation, collected from the subsurface Akkas-1 exploration well (with sample depths ranging from 2335 to 4130 meters) in western Iraq. These shales (sample prefix "AK1KHSH") were reported to have properties typical of oxic depositional environments and contained relatively low organic content (TOC 0.04–0.84%), making them quite different from the black shales of the Oslo Region (described in Chapter 2). However, they were still included in this study to evaluate the robustness of the norm calculations in SlateNorm used on data with varying geochemical compositions.

Dataset 2: Qingshankou Formation, Songliao Basin, Northeast China – Hu et al. (2021)

The second dataset consists of eight core samples from the Lower Cretaceous (145–100 Ma) Qingshankou Formation in the southern Songliao Basin, northeast China. These samples (sample prefix "ZS3") were collected from a drill core at depths ranging from 779 to 824 meters.

These samples are described as dark-gray mudstones interlayered with oil shales, deposited in semi-deep to deep lake conditions under reducing conditions. As such, the depositional environment of these samples is similar to the black shale units found in the Oslo region.

Dataset 3: Lower Cambrian black shale profiles, Northeast Chongqing, China – Ling et al. (2016)

The third dataset consists of 32 samples collected from a total of three weathering profiles (sample prefix "A", "B", and "C") developed within the Lower Cambrian (541–485 Ma) black shales located in Northeast Chongqing, China. These samples were obtained from recently exposed engineering cuttings at different positions along a hillslope gradient. These black shales were found to contain a relatively high amount of organic matter, and sulphides (mainly pyrite).

Dataset 4: Lower Ordovician Alum Shale, Northwestern Estonia, Baltic Palaeobasin – Vind et al. (2023)

The fourth dataset consists of 95 samples collected from a total of four drill cores (sample prefix "F298", "F330", "F343", and "F344") that intersect the Lower Ordovician (485–478 Ma) Alum Shale formation in northwestern Estonia. As noted in their published research, this formation is "an eastward continuation of the Cambrian-to-Ordovician black shales that extend from the Oslo region in Norway to NW Russia" (Vind et al., 2023, p. 2). For a more extensive description of this formation in Norway, see Chapter 2.

6.2. Compilation of datasets

The overview spreadsheet (Appendix A) includes: (1) study, locality and sample ID(s); (2) full bulk composition; (3) the same values reformatted for SlateNorm input; (4) the calculated norm mineralogy; (5) reported XRD mineralogy; and (6) the absolute relative percentage difference between SlateNorm and XRD results.

6.2.1. Modification of geochemical data

Since none of the datasets meet the exact input requirements of SlateNorm, several modifications were made to the raw geochemical data. To ensure consistency across datasets and compatibility with the SlateNorm algorithm, the following modifications were applied across the datasets where needed:

(1) Total organic carbon was used to directly represent organic carbon [C(org)], based on the standard assumption that TOC reflects only non-carbonate carbon following acid treatment (Bisutti et al., 2004). Most samples included in this study are organic-rich black shales, typically formed in anoxic, low-carbonate depositional environments.

(2) While XRD analyses shows trace occurrences of calcite and dolomite in some samples, these carbonate minerals are generally present at very low concentrations across datasets (average of <3 wt.%). Therefore, the CO_2 input variable, which was not consistently reported in the compositional data, was accordingly set to zero in all SlateNorm inputs. This allowed a realistic evaluation of the model's ability to calculate mineralogy from chemical composition alone, operating without prior mineralogical knowledge. However, this did result in SlateNorm calculating 0 wt.% for all carbonate minerals across datasets (Step 4; Chapter 5.1.2.).

(3) To ensure further consistency across input data from samples collected under different conditions (e.g., weathered outcrops versus fresh drill cores), and to better represent the original, unoxidized state of the rock, all reported iron was converted from Fe_2O_3 to FeO using a stoichiometric factor ($Fe_2O_3 \times 0.8998$). This adjustment supports the objective of estimating the mineralogy prior to surface alteration, which is especially relevant when assessing the potential for acid rock drainage.

(4) As mentioned in section 5.1.1., defining S as elemental S rather than SO_3 is required by the SlateNorm algorithm (Wagner et al. 2020). Therefore, reported SO_3 values, where present, were converted to elemental S by using a stoichiometric factor ($SO_3 \times 0.4003$). Similarly, titanium reported as elemental Ti was converted to titanium dioxide TiO_2, as required for SlateNorm input, using a stoichiometric factor ($Ti \times 1.6681$).

(5) Some of the required geochemical data were originally reported in parts per million (ppm), while the SlateNorm model requires all input values to be in weight percent (wt.%).

To ensure compatibility, all ppm values were converted to wt.% by dividing by 10,000 (i.e., 10,000 ppm = 1 wt.%). This step was applied consistently across all relevant parameters to standardize input formats.

(6) As mentioned in Section 5.1.3, it was found through initial testing that, although SlateNorm includes H_2O^+ as an input variable, this value does not influence the outcome of the normative mineral calculation. While H_2O^+ could be estimated from reported LOI values and included in the input data, the parameter was set to zero across all datasets due to its lack of effect on the model results. This decision ensures consistency and avoids introducing uncertainty from LOI-based H_2O^+ estimates that have no functional impact on the final calculations.

(7) *Dataset 1* was reported to have relatively low organic content (TOC of 0.04–0.84 wt.%; Al-Juboury et al.,2020). Additionally, TOC values were not provided as raw data in the original publication, but only as a general range, meaning they could not be directly included in the calculations at a per sample basis. As a result, given that this dataset differs substantially from the others in both geochemistry and depositional context (relatively much lower TOC content), the C(org) parameter was set to zero for all samples in this dataset.

7. Results

In this chapter, results of using SlateNorm to determine and quantify shale mineralogy is reported and compared with XRD analysis results, this includes: (1) absolute relative percentage difference of individual minerals and mineral groups present in the published XRD results for each dataset. (2) Mineral quantities from each method are compared using Lin's CCC (r_c) with 95% CIs for each dataset. And (3) a comprehensive scatterplot with all samples, plotting the absolute relative percentage difference between SlateNorm and XRD wt.% against XRD wt.% with an included accuracy threshold line to highlight large deviations from expected performance across varying mineral concentrations.

Comparisons were made directly between the two methods where possible (e.g., quartz vs. quartz). However, as previously discussed (Table 4; Chapter 5.1.1.), SlateNorm outputs a specific mineralogy. These outputs may not always be consistent with reported XRD mineralogy. For example, feldspars are calculated as anorthite, albite, and orthoclase in SlateNorm, while XRD results typically report feldspars more broadly (e.g., as alkali feldspar and plagioclase). Therefore, feldspar results were grouped following Wagner et al. (2020; Table 4) where possible as "feldspars". When XRD reported only general categories (e.g., plagioclase), comparisons were made only against the summed relevant SlateNorm outputs (e.g., albite + anorthite for plagioclase).

7.1. Absolute relative difference

Charts were generated for every included mineral or mineral group in all four datasets; a representative subset is shown below (for full set of charts, see Appendix B). Samples with SlateNorm output = 0 wt.% or extreme outliers (Chapter 5.2) are omitted here. Complete numeric results including the excluded samples are provided in Appendix A. Also note that the blue lines connecting data points (absolute relative difference) in the following charts are included for improved visual clarity only, these lines do not represent continuous data or trends between individual sample points.

SlateNorm chlorite estimates show a systematic bias for over-estimating concentrations, with absolute relative difference values exceeding XRD by >100% in nearly all samples across datasets, included here are several outliers overshooting by >1000%. Note that most XRD chlorite concentrations are below 10 wt.% (Fig. 5).
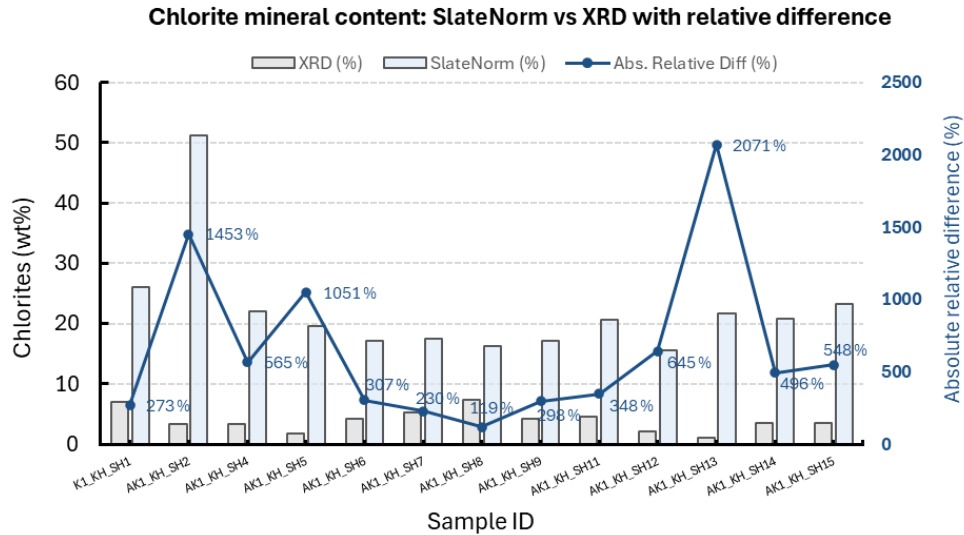
Figure 5: *Comparison of chlorite wt.% determined by SlateNorm and XRD, with absolute relative difference, for 13 shale samples (Dataset 1; Khabour Formation, Iraq; Al-Juboury et al., 2020).*

SlateNorm clay mineral estimates shows a systematic bias for under-estimating mineral concentrations, with results relatively lower than XRD values by >30% in nearly all samples across datasets, or even more as shown in the following chart (Dataset 2; Fig. 6).
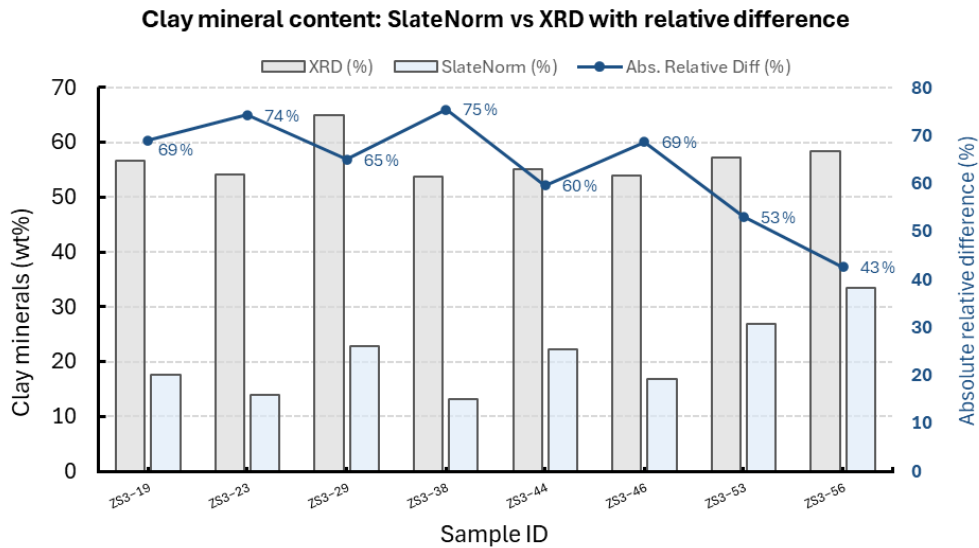

Figure 6: *Comparison of clay mineral wt.% determined by SlateNorm and XRD, with absolute relative difference, for 8 shale samples (Dataset 2; Qingshankou Formation, China; Hu et al., 2021).*

SlateNorm feldspar estimates differ only slightly from XRD in some samples (<10% difference) but severely overshoots in others (>100%). The largest deviations come from overestimating concentrations, especially in samples with relatively low XRD concentrations. However, both under- and over-estimations occur across datasets (Fig. 7).
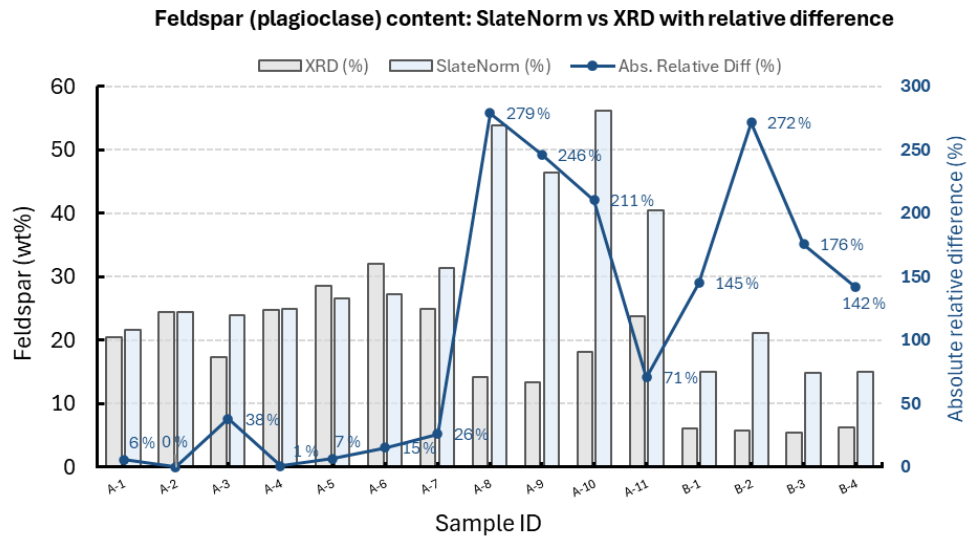

Figure 7: Comparison of plagioclase feldspar wt.% determined by SlateNorm and XRD, with absolute relative difference, for 15 black shale samples (Dataset 3; Lower Cambrian shale, China; Ling et al., 2016).

SlateNorm pyrite estimates differ from XRD by <10% in a few samples, but deviate by >30% in several others, especially in samples where XRD pyrite concentrations are relatively low. There are both over- and under-estimations of pyrite content across datasets (Fig. 8).
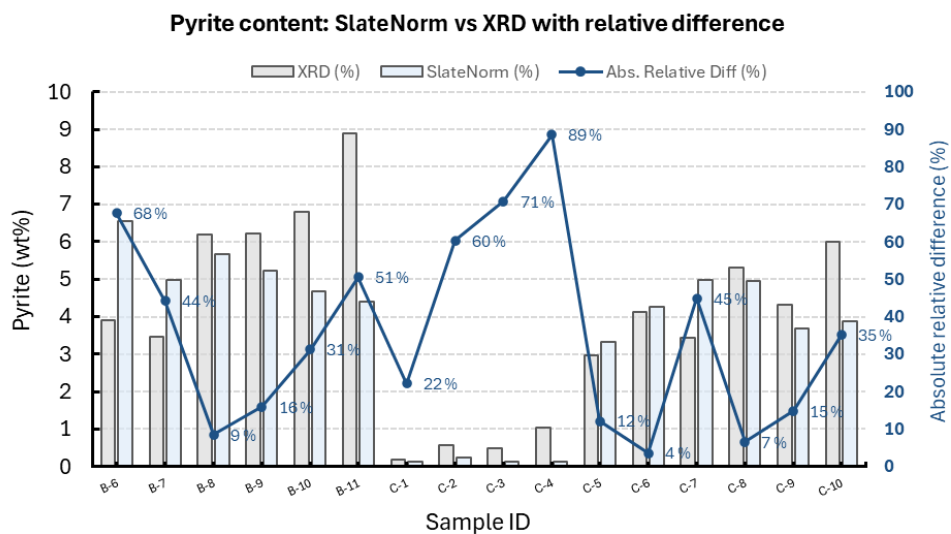

Figure 8: Comparison of pyrite wt.% determined by SlateNorm and XRD, with absolute relative difference, for 15 black shale samples (Dataset 3; Lower Cambrian shale, China; Ling et al., 2016).

SlateNorm quartz estimates range from near matches with XRD (<10% difference) to larger deviations (>30%), including both under- and over-estimations with no consistent trend across datasets (Fig. 9)
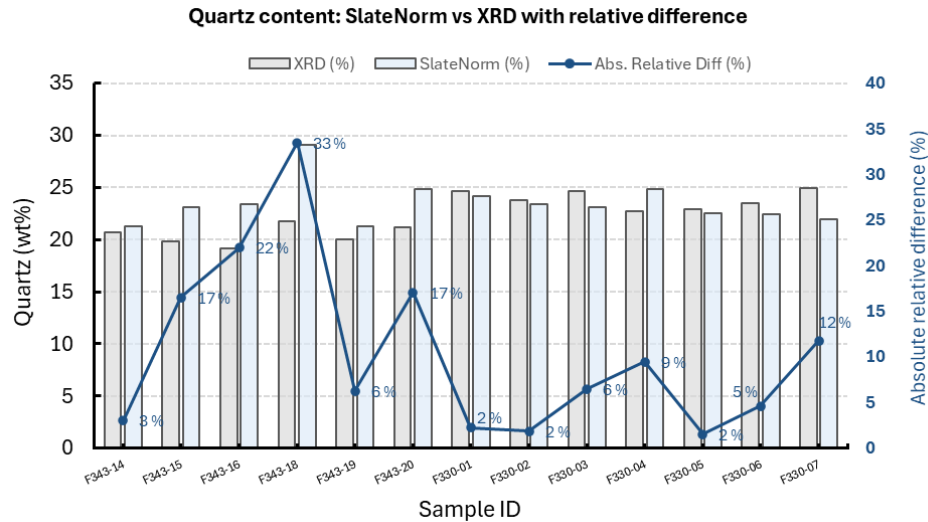

Figure 9: Comparison of quartz wt.% determined by SlateNorm and XRD, with absolute relative differences, for 13 Alum Shale samples (Dataset 4; Alum Shale Formation, Estonia; Vind et al., 2023).

7.2. Lin's Concordance Correlation Coefficient

Lin's r_c was calculated for all included minerals or mineral groups in each dataset. These plots, with 95% CIs are shown below. A minimum concordance correlation coefficient "threshold" (0.70) discussed in Chapter 5.2. is also included as a horizontal line in each chart.

Dataset 1: Cambro-Ordovician Khabour Formation, Iraq

Lin's r_c values stay below $r_c = 0.70$ for available minerals, only pyrite's 95% CI intersects the threshold. However, the CI for pyrite is wide and only based on six samples. (Fig. 10).
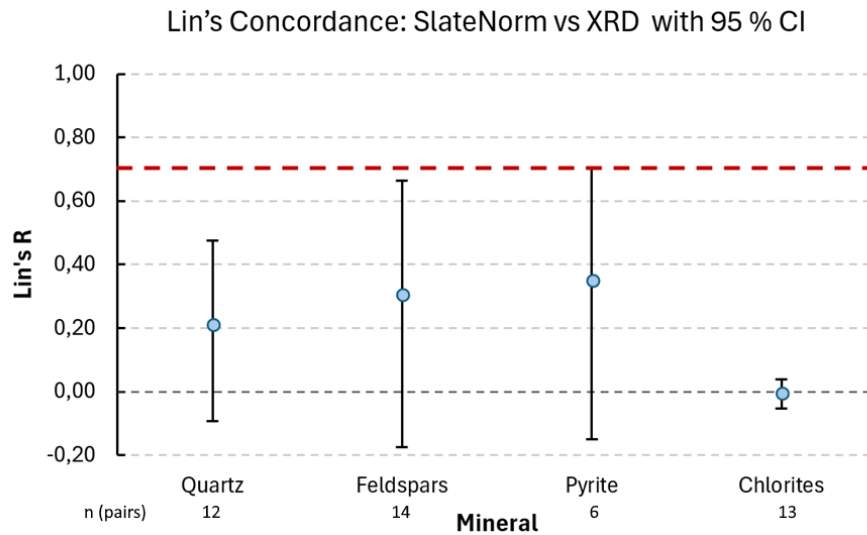
Figure 10: *Lin's CCC values for each mineral (blue dots) comparing SlateNorm to XRD with 95% confidence interval (black vertical lines) and minimum concordance correlation (red dashed line). n = pairs of compared results for each mineral (Dataset 1; Al-Juboury et al., 2020).*

Dataset 2: Qingshankou Formation, Songliao Basin, China

Lin's r_c values are well below $r_c = 0.70$ for every included mineral, all of which are based on eight samples (Fig. 11).
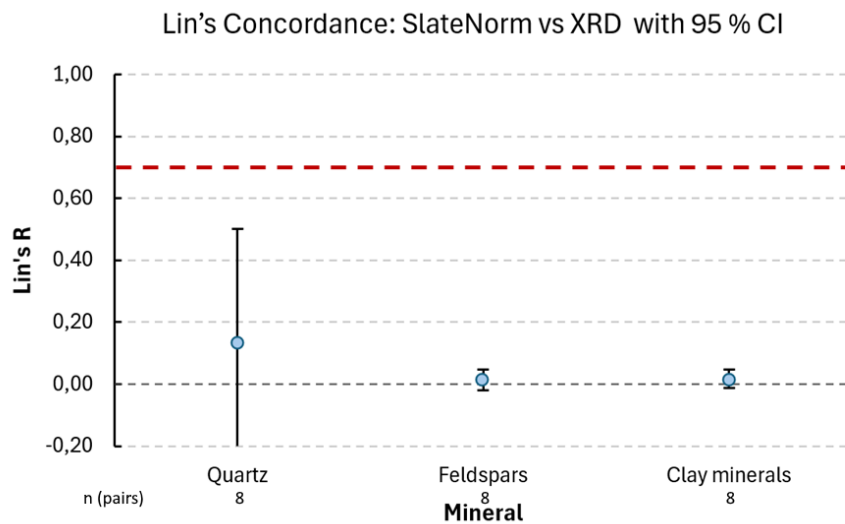

Figure 11: *Lin's CCC values for each mineral (blue dots) comparing SlateNorm to XRD with 95% confidence interval (black vertical lines) and minimum concordance correlation (red dashed line). n = pairs of compared results for each mineral (Dataset 2; Hu et al., 2021).*

36

Dataset 3: Lower Cambrian black shale profiles, Chongqing, China

Quartz and feldspar (n = 32 each) and muscovite (n = 23) all stay below the $r_c = 0.70$ threshold, whereas pyrite (n = 32) plots above the threshold at $r_c = \sim0.78$. CIs are generally narrower due to higher number of samples.
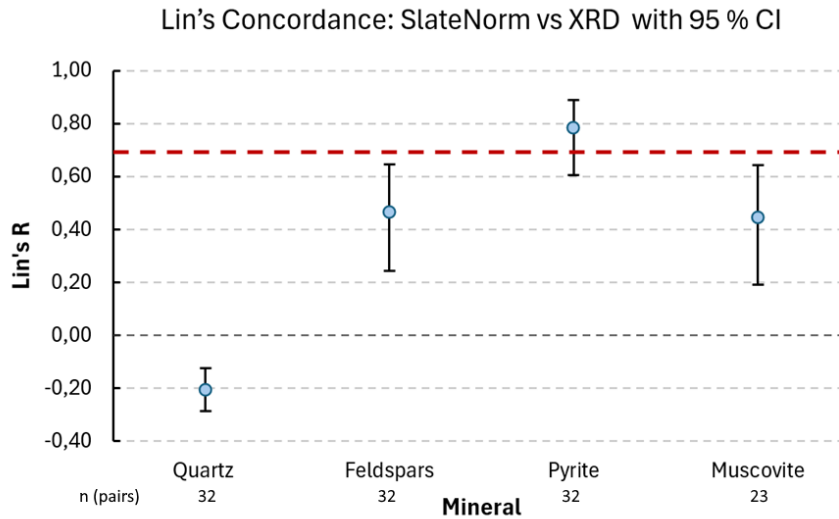

Figure 12: *Lin's CCC values for each mineral (blue dots) comparing SlateNorm to XRD with 95% confidence interval (black vertical lines) and minimum concordance correlation (red dashed line). n = pairs of compared results for each mineral (Dataset 3; Ling et al., 2016).*

Dataset 4: Lower Ordovician Alum Shale Formation, Baltic Palaeobasin, Estonia

Quartz and feldspar (n = 95 each) and chlorite (n = 79) all plot well below the $r_c = 0.70$ threshold, whereas pyrite (n = 95) plots just above it at $r_c = \sim0.71$, each with relatively tighter 95% CIs.
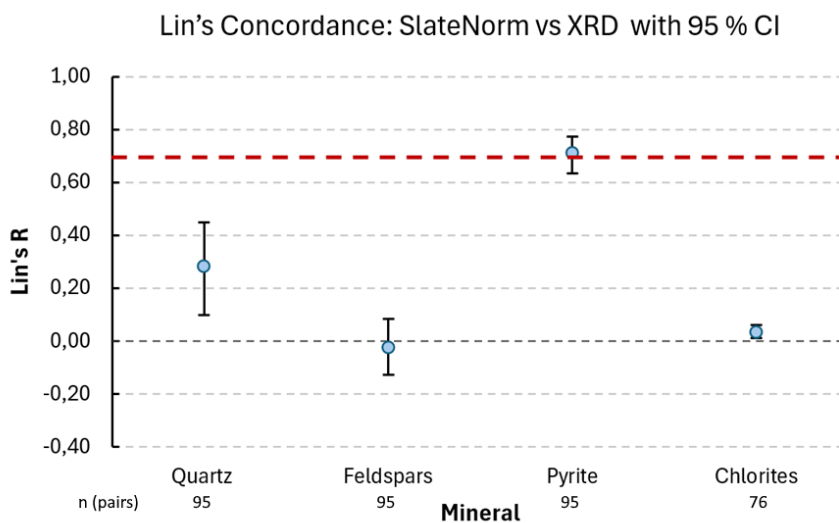

Figure 13: *Lin's CCC values for each mineral (blue dots) comparing SlateNorm to XRD with 95% confidence interval (black vertical lines) and minimum concordance correlation (red dashed line). n = pairs of compared results for each mineral (Dataset 4; Vind et al., 2023).*

7.3. Whole-dataset scatterplot

The combined scatterplot (Fig. 14) shows 481 mineral–sample pairs, with the absolute relative difference between SlateNorm and XRD versus XRD wt.% for each mineral within each sample. The cut off for y-values was set to 200%, which excludes the 61 most extreme outliers (> 200% relative difference).

Using this cutoff, 111 pairs or 23% are above the accuracy threshold. By including *all* pairs above the threshold (171 pairs), this amount increases to 31%. In general, deviations above the threshold occurs for both low and high XRD mineral concentrations.

Carbonate minerals are absent because the available comparable data contained either only trace amounts below XRD detection limits, or relatively very low amounts (average <3%). In addition, SlateNorm systematically calculated zero wt.% across output carbonate minerals due to how input data was imported (Chapter 6.2.1.).
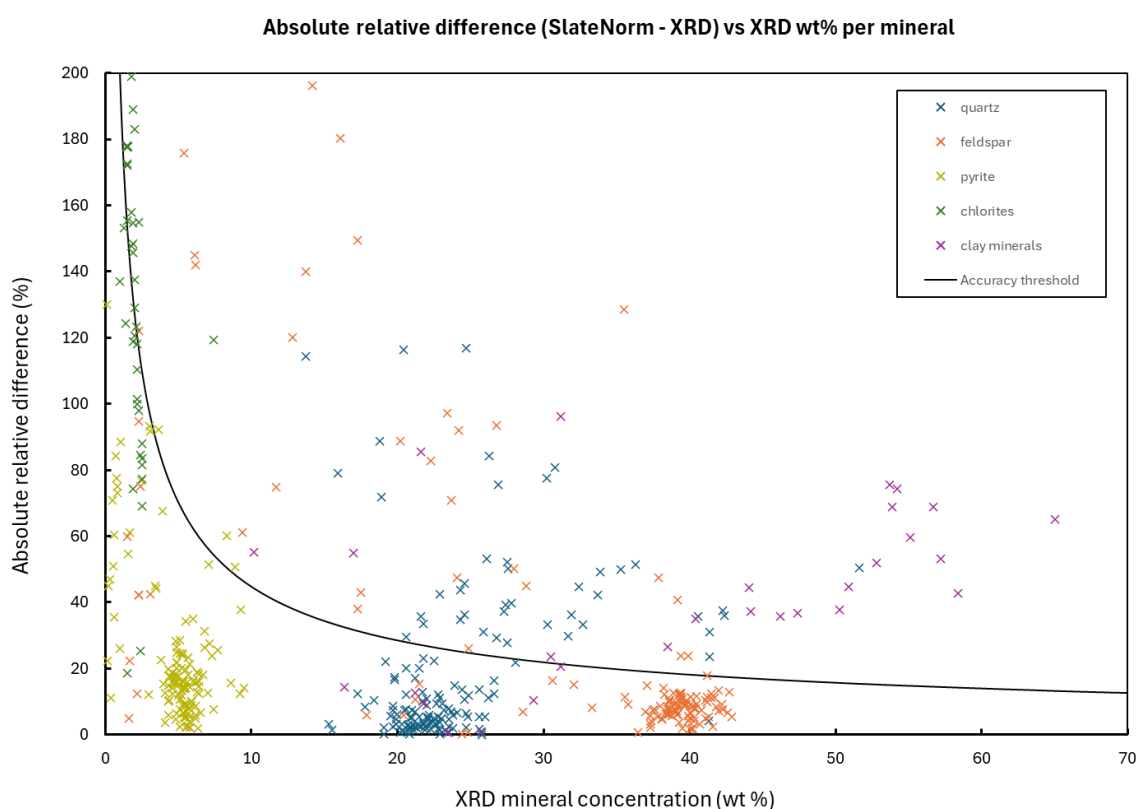

Figure 14: *Absolute relative percentage difference between SlateNorm wt.% and XRD wt.% plotted against XRD mineral concentrations wt.% for each mineral in a total of 481 mineral-sample pairs. Modified after Casetou-Gustafson et al. (2018). An acceptance threshold of ±200X$^{-0.65}$ (black line; modified version of XRD 95% CI; Hillier 2003) is also included.*

8. Discussion and future work

The aim of this study was to test how closely SlateNorm outputs, a CIPW-style normative algorithm developed for roofing slates (Wagner et al., 2020), compares with mineral quantities determined by quantitative XRD in four shale datasets. Across 481 mineral–sample pairs, 23% exceed the accuracy threshold (Hillier, 2003) which was artificially inflated to create some leeway. When the extreme outliers omitted from the whole-dataset scatterplot (Fig. 14) are included, that proportion rises to 31% or almost one third of calculated mineral-sample pairs. So in total, close to every third mineral calculated results in unacceptable over- or under-exaggerations. This brings into question the functionality of SlateNorm for real-world applications.

Quartz, chlorite and the clay minerals cause most of these larger deviations, with deviations in worst cases exceeding >1 000%. While feldspar, pyrite and quartz plot more consistently within the modified Hillier (2003) threshold (Fig. 14), and in direct comparisons of quantities (Fig. 7-9, respectively) sometimes within ±10% of XRD, there are no consistent bias for over- or under-estimations. Additionally, deviations occur across all mineral concentrations which may point to random/unspecified errors in SlateNorm outputs. However, it may also a reflection of the quality of the input data, despite efforts in this study to ensure all data modifications were consistent and logical.

Lin's concordance correlation coefficients (Lin, 1989; Fig. 10-13) confirm the same picture. In three of the four datasets every compared mineral plots below $r_c = 0.70$; only pyrite in the Lower Cambrian- ($r_c \approx 0.78$; n = 32) and Alum Shale-datasets ($r_c \approx 0.71$; n = 95) clears the minimal threshold, which is already well below the suggested $r_c = 0.90$ threshold suggested for good correlation (McBride, 2005). Larger sample size (Dataset 3, 4) tightens the confidence intervals but do not show good correlation in any other mineral. Quartz and feldspars (n = 95), and chlorite (n = 76) still gives poor overall results, further indicating SlateNorm's relatively weak overall performance in this study.

8.1. Likely causes of underperformance

SlateNorm's underperformance may be due to the algorithm itself, which uses the same step-by-step rules for splitting oxides into minerals as the original CIPW norm (Cross et al., 1902), a method created for less complex, anhydrous igneous rocks. When using a similar "static"

method on organic-rich, hydrous shales the chemical assumptions may be more likely to produce misleading results, especially for minerals with structural OH$^-$ or interlayer water (clays, chlorite). This assumption is further back up by the fact that the program asks for a bound-water (H2O+) input but ignores it. This may cause error when SlateNorm is assigning elements such as Al, Si, Fe and Mg to either chlorites or clay minerals, which might explain over- and under-estimates of those minerals (Fig. 5; Fig. 6, respectively).

For the reason previously specified (Chapter 6.2.1.), some alterations were consistently made to input data. The applied "rule" of setting $CO_2 = 0$ across all input data essentially means carbonate minerals are switched off in SlateNorm outputs (CO_2 is assigned to carbonate minerals in the underlying algorithm; Wagner et al., 2020). This forces SlateNorm to assign CaO and MgO inputs into other minerals such as feldspars and chlorites, artificially inflating their calculated quantities. Additionally, the applied stoichiometric conversions (Chapter 6.2.1.) may be unrealistic in that the reduction of Fe_2O_3 to FeO and of SO_3 to elemental S assumes redox states that may not align perfectly with the samples or their XRD results. Every mis-assignment here could potentially cause compounding errors in the algorithm as it goes through the following steps for assigning remaining oxides and elements to the predefined mineral outputs.

However, these are only *best guesses* as to why SlateNorm performed poorly in this study. The software itself is closed-source, lacks proper documentation and has not been cited in peer-reviewed work beyond its original roofing-slate study (Wagner et al., 2020). Therefore, general bugs and errors in the program itself cannot be ruled out. Moreover, the algorithm was treated here as a black box. Its internal chemical assumptions were not investigated in detail, because that lay far outside the scope of this study, which is a further limiting factor for any firm conclusion of the problem.

8.2. Impact of XRD reference data

Quantitative XRD itself carries ca. 5 wt.% absolute error for major minerals, and even less accuracy for trace amounts and non-crystalline (amorphous) material (Hillier, 2000; Lou et al., 2020). But those uncertainties are still much smaller than the relatively common bad outliers observed here (e.g., difference of >200% in several direct comparisons; Fig. 5, Fig. 7), so XRD uncertainty alone cannot explain the much larger, seemingly random deviations of SlateNorm-calculated mineralogy produced here. Nevertheless, for minerals that make up

low quantities in XRD results, such as chlorite in Dataset 1 (avg. <5 wt.%) or pyrite in Dataset 4 (avg. <6 wt.%), the XRD values themselves are so uncertain that it's hard to tell whether SlateNorm is really off, or the reference XRD values are just too uncertain.

8.3. Implications for environmental assessments

Because SlateNorm cannot consistently quantify key minerals in shales that drive ARD, notably pyrite and pyrrhotite, and the main carbonate minerals that buffer it, calcite and dolomite (Bjørlykke, 1974; Dold, 2017), any ARD predictions based on its output are likely to be very misleading. SlateNorm's frequent large and erratic errors in quartz and clay estimations also matter here, because the quartz-to-clay ratio determines rock brittleness: more brittle rocks fracture more easily, which can increase surface water infiltration and accelerate sulphide oxidation (Bailey et al., 2022; Dold, 2017; Rimstidt et al., 2017). Taken together, these shortcomings mean SlateNorm is not a practical tool for mineral shale mineral identification, quantification, or ARD assessments in its current form.

8.4 Future work

Mineral identification and quantification of shale remains a problem. This study has demonstrated that mineral norm calculations using SlateNorm, although promising in theory, is not giving reliable results in the context presented here. Based on identified limitations and these results, some clear improvements could be made to SlateNorm or a software like it to potentially improve norm calculated mineralogy: The algorithm must correctly incorporate structural water (H_2O^+) to accurately quantify hydrous minerals such as clays and chlorites, and outputs needs to be expanded to include pyrrhotite ($Fe_{(1-x)}S$). Also, future validation of mineralogical outputs should be done against high-resolution methods like Automated Mineralogy Systems in order to strengthen the assumption that compared mineralogy reflects real mineralogy.

The overall most reliable method probably involve the Automated Mineralogy Systems as discussed in Chapter 4.2. However, these methods are expensive and time consuming, in particular if it needs to be applied at a large scale like for the alum shale in Norway. Despite these shortcomings, it may be useful to apply these systems, even at a smaller scale, to evaluate their usefulness for shale (e.g., alum shale) mineral quantification.

References

Al-Juboury, A. I., Howard, J., Thusu, B., Nichols, G., Vincent, S. J., Kaye, M. N. D., & Vautravers, B. (2020). Mineralogy, geochemistry and source potential of shale in the Cambro-Ordovician Khabour Formation, Iraq. *Journal of African Earth Sciences, 167*, 103839.

ALS Geochemistry. (2025). *ALS Geochemistry fee schedule*. Retrieved February 15, 2025, from https://www.alsglobal.com/en/geochemistry/geochemistry-fee-schedules

Bailey, A. H. E., Jarrett, A. J. M., Wang, L., Reno, B. L., Tenthorey, E., Carson, C., & Henson, P. (2022). Shale brittleness within the Paleoproterozoic Isa Superbasin succession in the South Nicholson region, northern Australia. *Australian Journal of Earth Sciences*, 1–18. https://doi.org/10.1080/08120099.2022.2095029

Bastiansen, R., Moum, J., & Rosenqvist, I. T. H. (1957). Bidrag til belysning av visse bygningstekniske problemer ved Oslo-områdets alunskifere. *NGI Publikasjon No. 22*, *Norges Geotekniske Institutt.* Retrieved January 19, 2025, from https://www.nb.no/maken/item/URN:NBN:no-nb_digibok_2012022208018/open

Bhartia, R., Beegle, L. W., DeFlores, L., Abbey, W., Hollis, J. R. et al. (2021). Perseverance's Scanning Habitable Environments with Raman and Luminescence for Organics and Chemicals (SHERLOC) investigation. *Space Science Reviews, 217*, 58.

Bisutti, I., Hilke, I., & Rassler, M. (2004). Determination of total organic carbon: An overview of current methods. *Trends in Analytical Chemistry, 23*(10–11), 716–726.

Bjørlykke, K. (1974). Depositional history and geochemical composition of Lower Palaeozoic epicontinental sediments from the Oslo region. *Norges geologiske undersøkelse Bulletin 305*, 1–81.

Carr, M. J., & Gazel, E. (2017). IGPET software for modeling igneous processes: Examples of application using the open educational version. *Mineralogy and Petrology, 111*, 283–289.

Casetou-Gustafson, S., Hillier, S., Akselsson, C., Simonsson, M., Stendahl, J., & Olsson, B. A. (2018). Comparison of measured (XRPD) and modeled (A2M) soil mineralogies: A study of some Swedish forest soils in the context of weathering rate predictions. *Geoderma, 97*(1–2), 77–88.

Cross, W., Iddings, J. P., Pirsson, L. V., & Washington, H. S. (1902). Quantitative classification of igneous rocks based on chemical and mineralogical composition. *U.S. Geological Survey Bulletin No. 209*, 284.

Dold, B. (2017). Acid rock drainage prediction: A critical review. *Journal of Geochemical Exploration, 172*, 120–132.

Gleisner, M., & Herbert, R. B., Jr. (2002). Sulfide mineral oxidation in freshly processed tailings: Batch experiments. *Journal of Geochemical Exploration, 76*(3), 139–153.

Gomo, M. (2018). Conceptual hydrogeochemical characteristics of a calcite and dolomite acid mine drainage neutralised circumneutral groundwater system. *Water Science, 32*(2), 355–361.

Goodge, J. (2018). Electron probe micro-analyzer (EPMA). *University of Minnesota–Duluth*. Retrieved March 7, 2025, from https://serc.carleton.edu/msu_nanotech/methods/EPMA.html

Epp, J. (2016). X-ray diffraction (XRD) techniques for material characterization. *Materials Characterization Using Nondestructive Evaluation (NDE) Methods, 81-124.*

Hillier, S. (2000). Accurate quantitative analysis of clay and other minerals in sandstones by XRD: Comparison of a Rietveld and a reference intensity ratio (RIR) method and the importance of sample preparation. *Clay Minerals, 35*(1), 291–302.

Hillier, S. (2003). Quantitative analysis of clay and other minerals in sandstones by X-ray powder diffraction (XRPD). *International Association of Sedimentologists Special Publication*, 34, 213–251.

Hu, F., Meng, Q., & Liu, Z. (2021). Mineralogy and element geochemistry of oil shales in the Lower Cretaceous Qingshankou Formation of the southern Songliao Basin, northeast China: Implications of provenance, tectonic setting, and paleoenvironment. *ACS Earth and Space Chemistry, 5*, 365–380.

Hurum, J. H., & Frøyland, M. (2004). Chapter 4. Nedre Eikers underjordiske skatter: Stein til nytte og glede. *Nedre Eiker kommune*, 113–118.

Janzen, M. P., Nicholson, R. V., & Scharer, J. M. (2000). Pyrrhotite reaction kinetics: Reaction rates for oxidation by oxygen, ferric iron, and for nonoxidative dissolution. *Geochimica et Cosmochimica Acta, 64*(9), 1511–1522.

Khan, H., Yerramilli, A. S., D'Oliveira, A., Alford, T. L., Boffito, D. C., & Patience, G. S. (2019). Experimental methods in chemical engineering: X-ray diffraction spectroscopy—XRD. *The Canadian Journal of Chemical Engineering, 97*(11), 2656–2665.

Lin, L. I.-K. (1989). A concordance correlation coefficient to evaluate reproducibility. *Biometrics, 45*(1), 255–268.

Ling, S., Wu, X., Sun, C., Liao, X., Ren, Y., & Li, X. (2016). Mineralogy and geochemistry of three weathered Lower Cambrian black shale profiles in northeast Chongqing, China. *Geosciences Journal, 20*(5), 639–653.

Lou, W., Zhang, D., & Bayless, R. C. (2020). Review of mineral recognition and its future. *Applied Geochemistry, 122*, 104727.

Mcbride, G. B. (2005) A proposal for strength-of-agreement criteria for Lin's Concordance correlation coefficient. *NIWA client report: HAM2005-062.*

Nakrem, H. A., & Worsley, D. (2013). Chapter 5. Landet blir til – Norges geologi. *Norsk Geologisk Forening*, 151–179.

Nicholson, R. V., & Scharer, J. M. (1994). Laboratory studies of pyrrhotite oxidation kinetics. *American Chemical Society, 550*, 14–30.

Nielsen, A. T., Schovsbo, N. H., Klitten, K., Woollhead, D., & Rasmussen, C. M. Ø. (2018). Gamma-ray log correlation and stratigraphic architecture of the Cambro-Ordovician Alum Shale Formation on Bornholm, Denmark: Evidence for differential syndepositional isostasy. *Bulletin of the Geological Society of Denmark, 66*, 237–273.

Oyedotun, T. D. T. (2018). X-ray fluorescence (XRF) spectrometry: An overview of sample preparation methods for geological materials. *Applied Spectroscopy Reviews, 53*(9), 707–730.

Pabst, T., Sørmo, E., & Endre, E. (2016). Geochemical characterisation of Norwegian Cambro-Ordovician black mudrocks for building and construction use. *Bulletin of Engineering Geology and the Environment, 75*(4), 1527–1543.

Pelkonen, M. K., Reinoso-Maset, E., Law, G. T. W., Lind, O. C., & Skipperud, L. (2025). Environmental impact of an acid-forming alum shale waste rock legacy site in Norway. *Environmental Science: Processes & Impacts, 27*(2), 225–238.

Pownceby, M. I., MacRae, C. M., & Wilson, N. C. (2007). Mineral characterisation by EPMA mapping. *Minerals Engineering, 20*(5), 444–451.

Raman, C., & Krishnan, K. (1928). A new type of secondary radiation. *Nature, 121*(3051), 501–502.

Rimstidt, J. D., Chermak, J. A., & Schreiber, M. E. (2017). Processes that control mineral and element abundances in shales. *Earth-Science Reviews, 171*, 383–399.

Ro, H. E., Larsson, F. R., Kinck, J. J., & Husebye, E. S. (1990). The Oslo Rift—Its evolution on the basis of geological and geophysical observations. *Tectonophysics, 178*(1), 11–28.

Rollinson, G. K., Andersen, J. C. Ø., Stickland, R. J., Boni, M., & Fairhurst, R. (2011). Characterisation of non-sulphide zinc deposits using QEMSCAN. *Minerals Engineering, 24*(8), 778–787.

Rostron, P., Gaber, S., & Gaber, D. (2016). Raman spectroscopy review. *International Journal of Engineering and Technical Research, 6*(1), 12–18.

Sauerer, B., Craddock, P. R., AlJohani, M. D., Alsamadony, K. L., & Abdallah, W. (2017). Fast and accurate shale maturity determination by Raman spectroscopy measurement with minimal sample preparation. *International Journal of Coal Geology, 173*, 150–157.

Secchi, M., Zanatta, M., Borovin, E., Bortolotti, M., Kumar, A., Giarola, M., Sanson, A., Orberger, B., Daldosso, N., Gialanella, S., Mariotto, G., Montagna, M., & Lutterotti, L. (2018). Mineralogical investigations using XRD, XRF, and Raman spectroscopy in a combined approach. *Journal of Raman Spectroscopy, 49*(7), 1137–1144.

Vind, J., Ofili, S., Mand, K., Soesoo, A., & Kirsimae, K. (2023). Redox-sensitive trace metal hyper-enrichment in Tremadocian Alum Shale (graptolite argillite) in northwestern Estonia, Baltic Palaeobasin. *Chemical Geology, 640*, 121746.

Wagner, H. W., Jung, D., Wagner, J.-F., & Wagner, M. P. (2020). Slatecalculation—A practical tool for deriving norm minerals in the lowest-grade metamorphic pelites and roof slates. *Minerals, 10*(11), Article 964.

Wagner, H. W. (2022). Normative mineralogy especially for shales, slates and phyllites. *IntechOpen, Mineralogy.* https://doi.org/10.5772/intechopen.102346

Zaiontz, C. (2025). Real statistics resource pack [Excel add-on]. Retrieved February 2, 2025, from https://real-statistics.com/free-download/

Zimmerman, R. W., & Bodvarsson, G. S. (1996). Hydraulic conductivity of rock fractures. *Transport in Porous Media, 23*(1), 1–30. https://doi.org/10.1007/BF00145263